

# **Abstract**



# Acknowledgements



# Contents

<b>1</b>	<b>Introduction</b>	<b>7</b>
<b>2</b>	<b>Theory</b>	<b>11</b>
2.1	Spin-orbit coupling . . . . .	11
2.2	Wannier Functions . . . . .	11
<b>3</b>	<b>Spin-momentum locking in high spin-orbit coupled ferroelectrics</b>	<b>13</b>
3.1	Introduction . . . . .	13
3.2	Rashba-Bychkov Effect . . . . .	14
3.3	Orbital Rashba Effect . . . . .	16
3.3.1	Tight-Binding model . . . . .	17
3.4	Overview: Germanium Telluride . . . . .	21
3.5	Methods . . . . .	21
3.6	Band structure . . . . .	21
3.7	Results and Discussion . . . . .	22
3.8	Conclusions . . . . .	23
<b>4</b>	<b>Coupling between spin and strain density waves</b>	<b>29</b>
4.1	Introduction . . . . .	29
4.2	Experimental methods . . . . .	29
4.3	Theory . . . . .	30
4.4	Results . . . . .	31
<b>5</b>	<b>Topological Multiferroic switching; coupling between Magnetism and Ferroelectricity in GdMn<sub>2</sub>O<sub>5</sub></b>	<b>37</b>
5.1	Introduction . . . . .	37
5.2	GdMn <sub>2</sub> O <sub>5</sub> . . . . .	37
5.3	Theory . . . . .	38
5.4	Simplified Model . . . . .	41
<b>6</b>	<b>Mechanical softening in Ferroelectric domain walls</b>	<b>47</b>
6.1	Introduction . . . . .	47
6.2	Experimental . . . . .	47
6.3	Theory . . . . .	48
6.4	Results . . . . .	49
<b>7</b>	<b>Strong coupling and ultrafast control of charge and spin density waves in elemental Chromium</b>	<b>53</b>



# Chapter 1

## Introduction

Theoretical condensed matter research is plagued by a fundamental issue of complexity. The shear amount of degrees of freedom in a material of any technologically relevant scale is overwhelming (i.e.  $\sim 10^{23}$  electrons per  $\text{cm}^3$ ), and make it impossible to describe the quantum mechanical wavefunction exactly [there is some more nice things along this line in Wen]. This forces researchers in the field to make approximations, as to make the problem tractable, while still capturing the essential physics resulting in the effects under investigation.

The way to make progress with this undertaking has always been to try and isolate the parts of the system that contribute the most. As is well known, every quantum mechanical system is governed fundamentally by its Hamiltonian. One could go so far as to say that if we would be able to exactly calculate all of its eigenvectors and eigenvalues, the field of condensed matter would be completed. This is of course impossible for reasons stated above.

The full Hamiltonian can be decomposed into several contributions, which allows one to focus on the most important contributions, while discarding the rest. For example, the elastic energy scales needed to completely break a material, while important for mechanical studies, are so much larger than those governing the movement of electrons through the material, that they can be discarded if we are only interested in the latter.

What this means fundamentally is that we are separating the full Hilbert space of possible states that the full wavefunction system can assume into separate parts that each take care of different aspects of the full physics. A relevant example is that the ionic response of a material can be described by phonons, these contribute very little to currents that may flow through it. Thus, while the full wavefunction and Hilbert space contains both the phonons and electrons, we can split it up into both parts, with an interaction between them. If this interaction is negligible, we can write the full wavefunction as the product of two parts in each of these spaces with no entanglement between them, and we can solve the physics of both parts separately.

If this procedure is carried out systematically, at some point we end up with something that is actually solvable, which will hopefully describe the biggest part of the observed behavior. This is essentially how the field of condensed matter has progressed starting from the most fundamental quantum mechanical laws, first focusing on exactly solvable constituent problems, gradually adding complexity in order to describe more complex physics.

In general, projects contained in this Thesis will focus on this step of taking two solved constituent problems, adding an interaction between them and observing what new physics emerge. There are three of these coupling interactions that will be discussed: spin-orbit coupling (SOC), exchange striction, and electrostriction. The focus will lie on electronic, magnetic and structural properties of ferroic crystals. In some of these materials, where multiple ferroic orders coexist (so-called multiferroics), the interactions will allow to influence either ferroic order by perturbing the other.

The SOC is a relativistic effect, that can often be ignored if one is interested in the electronic structure inside a crystal with light ions. In the case of GeTe, however, an anomalously large spin-splitting of two normally degenerate spin states, was found in the bandstructure of the ferroelectric material. Another result of this interaction is a fundamental coupling between the crystalline lattice and magnetism if it is present. This causes the usually isotropic magnetic interactions between the on-site spins, given by the Heisenberg exchange Hamiltonian  $\sum_{\langle i,j \rangle} J_{ij} \mathbf{S}_i \cdot \mathbf{S}_j$ , to become highly anisotropic, i.e. the coupling between the components of the spins depends on the direction of the bond:  $\sum_{\langle i,j \rangle, \mu, \nu} J_{ij}^{\mu\nu} S_i^\mu S_j^\nu$  where  $\mu, \nu = x, y, z$ . We will investigate Sr<sub>2</sub>IrO<sub>4</sub> in particular, where there is a strong SOC on the magnetic Ir atoms.

The second effect we will highlight is magnetic exchange striction, which stems from the dependence of exchange constants  $J_{ij}$  on structural distortions, leading to a coupling between the spins and phonons. This leads to a modulation of the magnetic configuration when phonons are present in the material, and vice versa to the creation of phonons when the magnetic interaction can gain energy if bond lengths are varied. Here we will highlight two specific situations. In the first, a ferroelectric polarization (a  $\mathbf{k} = \mathbf{0}$  phonon) emerges due to geometric frustration of anti-ferromagnetic ordering in GdMn<sub>2</sub>O<sub>5</sub>. The second situation is the well-known coupling between the spin density wave and charge density wave in elemental Chromium. In this case a peculiar nesting of the Fermi-surfaces results in a spin density wave to be stabilized, whereupon the exchange striction creates a charge density wave. It is this interaction that opens the path to a very precise control in ultrafast photoexcitation experiments of these collective modes, where the excitation of the spin density wave causes in turn an excitation in the charge density wave. The latter can then be controlled very precisely by further pulses, as is demonstrated in our work.

Lastly, the interaction between strain and ferroelectricity will be carefully studied in 180° domain walls in BaTiO<sub>3</sub>. This is one of the most well-known ferroelectric materials harboring a wide of ferroelectric phases, with very large polarization. Interestingly the coupling under discussion leads to a noticeable mechanical softening of 180° ferroelectric domain walls. This is not straightforward as the domain wall is not ferroelastic, i.e. it separates two domains with the same values for the strain tensor, making it not a priori clear why the purely ferroelectric wall appears softer. We will show that the electrostriction leads to a strain profile close to the wall which can interact with an atomic force microscopy tip, bending the wall towards it and thus appearing softer.

Aside from the purely academic interest, these interactions between separate parts of the systems also hold promise from a technological point of view. Due to these cross-couplings between degrees of freedom, as was alluded to before, it is possible to influence one part by perturbing the other. The most brought up case is that of hard disks, where the ferromagnetic domains that store the

data need to be reoriented by applying an external magnetic field, making it rather inefficient due to heating and limiting the data density caused by magnetic stray fields influencing multiple domains. If one would be able, however, to control the magnetic domains by applying an electric field, this would dramatically increase the efficiency. This is what makes multiferroics such as in our case  $\text{GdMn}_2\text{O}_5$ , are so interesting. The coupling between the ferroelectric polarization and magnetization in the material causes one to be able to change the latter by applying an electric field to the former. A thorough understanding of the switching behavior in this material is of paramount importance to utilize this effect efficiently. In the case of GeTe, as will discussed later, the spin polarization of the bands closest to the fermi level depend the direction of the ferroelectric polarization, thus theoretically allowing for a Datta Das transistor [citation!], allowing only a particular spin-polarized current to flow through the material.

In the case of the ferroelectric domain walls, the cross-coupling between strain and ferroelectricity allows to effectively move the ferroelectric domains by applying a strain field through a tip, due to the presence of very soft sliding modes.

[rundown of chapters here]



# Chapter 2

## Theory

### 2.1 Spin-orbit coupling

### 2.2 Wannier Functions

In a lot of the work presented in this Thesis we construct models to describe the physics that result in a certain effect in real materials. These models are most of the time defined in terms of a limited set of local atomic-like orbitals, since these offer the most intuitive understanding most of the time, and the biggest contribution to particular effects can often be traced back to only a limited subset of all the orbitals.

If we want to apply these models to real materials to get not only qualitative, but also quantitative results, we need to perform a fit to either experimentally obtained values, or first-principles simulations. The most feasible way is usually the latter, which requires us to find a bridge between the plane waves that are used in a lot of first-principles DFT codes, and the localized basis set of that the model is built from.

Wannier functions offer a rigorous and flexible solution to this question, rewriting the Bloch functions as a discrete Fourier transform of (exponentially) localized, cell-periodic wavefunctions.

This construction is flexible in the sense that it is not unique. Bloch functions have a gauge freedom at each  $k$  value, which in turn will have an effect on the Wannier functions. One gauge that is commonly used is the one that localized the functions as much as possible, leading to the so-called Maximally Localized Wannier Functions (MLWF). Other gauges can be chosen such that the obtained functions have certain symmetries or have maximum similarity to atomic orbitals.



# Chapter 3

## Spin-momentum locking in high spin-orbit coupled ferroelectrics

### 3.1 Introduction

The research field of spintronics aims to understand the behavior of spins inside materials, and translate this understanding into active control of these degrees of freedom for possible technological applications. Many possible devices have been theorized for example are spin field-effect transistors (spin-FET)[1] and storage devices which utilize spin-current and associated spin-transfer torque to efficiently manipulate magnetic domains [7, 6]. In spite of fundamental interest and potential for applications, the actual realization of these devices has been rather elusive. One of the main culprits for the limited success to date is that the devices require very granular, ideally electric, control of the spin, which is impeded by widely separated energy scales and weak coupling between magnetic and charge degrees of freedom. One class of materials that allow for such electric control of spin-polarized states are the ferroelectric semiconductors with large atomic spin-orbit coupling (SOC) [2, 5, 8]. Inversion symmetry breaking together with SOC results in a linear splitting of spin-polarized bands, seen in the band structure as a conical intersection surrounding a high-symmetry point of the Brillouin Zone (see Fig. 3.1). Thus, current carriers (holes in the case of Fig. 3.1) travelling through the material will tend to align their spins to these spin-polarized bands. As we discuss in more detail in the following, the direction of the spin polarization depends on the orientation and strength of the electric field  $\mathbf{E}$ . In ferroelectrics, an internal field results from the polarization  $P$ , allowing it to be tuned and switched by an external applied electric field. These spin-polarized states have been observed both experimentally [5, 10, 9], and from *ab-initio* density functional theory (DFT) simulations [2]. It is, however, often not well understood and often misattributed what the underlying microscopic mechanisms are that lead to the observed splitting. [explicit mentions? Maybe too aggressive]

We investigate multiple different origins of this  $k$  and  $E$  dependent spin-

splitting. The discussed contributions arise due to the Hamiltonian of form

$$H_R(\mathbf{k}) = \alpha_R \frac{\mathbf{E}}{|\mathbf{E}|} \cdot (\mathbf{k} \times \hat{\sigma}), \quad (3.1)$$

where  $\hat{\sigma}$  is the electron spin operator, and  $\mathbf{E}$  the electric field. It will turn out that multiple microscopic effects can lead to contributions of this form, some of these are well known, others are more obscure. The magnitude of the contribution depends on the microscopic origin, namely whether the effect is purely relativistic or rather a combination of relativistic and electrostatic. Certain materials showcase an exceedingly big splitting, for example in GeTe as can be seen in Fig. 3.1, and will be used as the main example throughout this chapter.

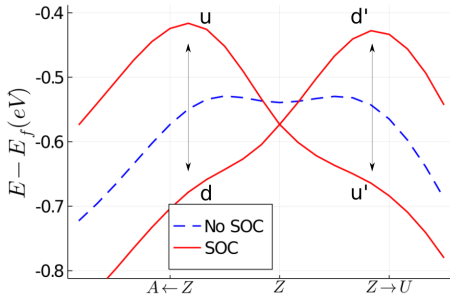


Figure 3.1: **Large Rashba splitting in GeTe** The two graphs show the band dispersions for the first valence band for the non spin-orbit coupled (NSOC, blue), and spin-orbit coupled (SOC, red) case, around the high-symmetry  $Z$  point of the Brillouin zone (see Fig. 3.4 for details). The  $u - d$  and  $u' - d'$  labels designate the up and down spin-polarized bands, where the prime signifies that the orientation of the spin axis depends on specific path followed in  $k$ -space.

We hope that this will shed light on where these contributions come from and how they compare with each other and how they ultimately lead to the observed spin-splitting.

### 3.2 Rashba-Bychkov Effect

The first discovered and most well known effect bearing the form of Eq. 3.1 is the Rashba-Bychkov effect, first derived in their seminal 1959 paper[15]. It is a relativistic effect that is derived from an expansion to second order in  $1/c$ ,  $c$  denoting the speed of light, of the electronic Dirac equation (where the Fouldy-Wouthuysen transformation was applied):

$$\mathcal{H}\psi = \left[ \frac{\mathbf{p}^2}{2m} - eV - \frac{e\hbar}{4m^2c^2} (\boldsymbol{\sigma} \cdot [\nabla V \times \mathbf{p}]) - \frac{\hbar^2}{8m^2c^2} \Delta V - \frac{\mathbf{p}^4}{8m^3c^2} \right] \psi = E\psi \quad (3.2)$$

where  $\psi$  is a two component spinor,  $V$  denotes the electric potential,  $\boldsymbol{\sigma}$  a vector of Pauli-matrices ( $\sigma_x, \sigma_y, \sigma_z$ ),  $m$  and  $e$  the electron mass and charge respectively, and  $\mathbf{p}$  the canonical momentum. The first two terms are the nonrelativistic part

of the Hamiltonian, the third represents the SOC, the fourth is known as the Darwin effect and the fifth is the relativistic correction to the effective electron mass. As is common in literature, we introduce the spin-orbit coupling constant  $\lambda = \frac{e\hbar}{4m^2c^2}$ . In a crystal with a periodic potential  $V(\mathbf{r})$ , electronic wavefunctions are Bloch wavefunctions  $\psi_n(\mathbf{k}, \mathbf{r}) = u_n(\mathbf{k}, \mathbf{r})e^{i\mathbf{k}\cdot\mathbf{r}}$ , where  $u_n$  denotes the cell-periodic part, and  $n$  is the band index. To obtain the eigenvalue equation for  $u_n(\mathbf{k}, \mathbf{r})$ , we insert  $\psi_n$  in Eq. 3.2, and carry out the differentiation  $\mathbf{p} e^{i\mathbf{k}\cdot\mathbf{r}} u_n(\mathbf{k}, \mathbf{r}) = e^{i\mathbf{k}\cdot\mathbf{r}} (\mathbf{p} + \mathbf{k}) u_n(\mathbf{k}, \mathbf{r})$ , and similarly  $\mathbf{p}^2 \rightarrow (\mathbf{p} + \mathbf{k})^2$ . This leads to the following equation for  $u_n(\mathbf{k}, \mathbf{r})$ :

$$E_n u_n(\mathbf{k}, \mathbf{r}) = (V_0 + V_1 + V_2 + V_3) u_n(\mathbf{k}, \mathbf{r}) \quad (3.3)$$

$$V_0(\mathbf{k}) = \frac{\mathbf{p}^2}{2m} - eV + \frac{\hbar^2 k^2}{2m} \quad (3.4)$$

$$V_1(\mathbf{k}) = \hbar \frac{\mathbf{k} \cdot \mathbf{p}}{m} \quad (3.5)$$

$$V_2(\mathbf{k}) = -\lambda \boldsymbol{\sigma} \cdot (\nabla V \times \mathbf{k}) \quad (3.6)$$

$$V_3(\mathbf{k}) = -\lambda \boldsymbol{\sigma} \cdot (\nabla V \times \mathbf{p}). \quad (3.7)$$

We neglected the last two terms of Eq. 3.2 since they are exceedingly small and don't contribute to the linear form of Eq. 3.1. It is important to understand how the electric fields inside the crystal contribute to  $V_2$  and  $V_3$ , where both terms originate from the application of  $\mathbf{p}$  to either  $u_n(\mathbf{k}, \mathbf{r})$  or  $e^{i\mathbf{k}\cdot\mathbf{r}}$ , respectively. We first separate  $\nabla V$  in two contributions, one coming from the potential wells created by the atoms, and another originating from the ferroelectric polarization (it is assumed that no external fields are applied):

$$\nabla V = \mathbf{E} = \mathbf{E}_{at} + \mathbf{E}_P \quad (3.8)$$

These contributions, together with the two parts of the Bloch functions (i.e. the cell periodic  $u_n(\mathbf{k}, \mathbf{r})$ , and envelope function  $e^{i\mathbf{k}\cdot\mathbf{r}}$ ) are pictorially shown in Fig. 3.2.

Looking at the picture, it becomes clear that the contribution of the atomic potential applied to the envelope function is zero because while  $k$  is a constant,  $E_{at}$  is odd throughout the unit cell, leading to the contributions on either side of the potential well to cancel out. Thus the only contribution to the first term in Eq. 3.9 comes only from the uniform (even)  $E_P$ , which in general is very small compared to the atomic one. A similar argument can be applied to the contribution to  $V_3$ . Here we can see that due to the shape of the periodic part of the wavefunction, only the contribution coming from  $E_{at}$  will be nonzero, this is essentially the well-known atomic spin-orbit coupling and can be rather large.

In the following it is assumed that Eq. 3.3 can be solved for a time reversal (TR) invariant point  $\mathbf{k}_0$  in the first BZ, where the two spin states are necessarily degenerate. Due to the broken inversion symmetry and inclusion of the SOC terms ( $V_2, V_3$ ), this degeneracy will be broken for  $k$  points away from the TR invariant point. We denote the two degenerate states at  $\mathbf{k}_0$  by  $|u_n^\downarrow\rangle$  and  $|u_n^\uparrow\rangle$ . It is important to realize that the orientation of spin axis of the eigenstates of Eq. 3.3 depends on the direction of both  $\mathbf{k}$  and  $\mathbf{P}$ , as will become clear later. Without loss of generality we can take  $\mathbf{k}_0 = \mathbf{0}$  and  $E_n^{\uparrow\downarrow}(\mathbf{0}) = 0$ . Expanding in the deviation away from the high-symmetry point, in the usual  $\mathbf{k} \cdot \mathbf{p}$  sense, and

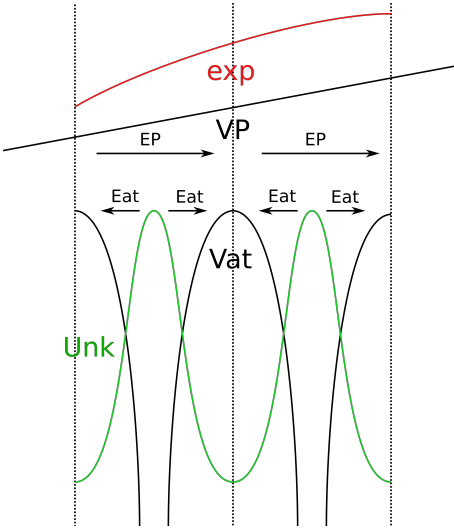


Figure 3.2: Pictorial representation of the different electric fields present in the crystal. The black lines denote the atomic potential and electric field,  $V_{at}$  and  $E_{at}$  respectively, and the contribution due to ferroelectricity,  $V_P$  and  $E_P$ . The green and red graphs denote the periodic ( $u(\mathbf{k}, \mathbf{r})_n$ ) and envelope part of the Bloch functions, respectively.

keeping only linear  $\mathbf{k}$  terms and terms up to second order in  $1/c$ , we get

$$E_n^{\sigma_1}(\mathbf{k}) = -V_2^{\sigma_1}(\mathbf{k}) + \quad (3.9)$$

$$\sum_{m, \sigma_2=\uparrow, \downarrow} \frac{\langle u_n^{\sigma_1} | V_1(\mathbf{k}) | u_m^{\sigma_2} \rangle \langle u_m^{\sigma_2} | V_3(\mathbf{k}) | u_n^{\sigma_1} \rangle + h.c.}{E_n^{\sigma_1} - E_m^{\sigma_2}}, \quad (3.10)$$

where the sum over  $m, \sigma_2$  includes all states which are not equal to  $n, \sigma_1$ .

Even though the latter term of Eq. 3.9 is of higher order in the perturbation theory, it usually has the same order of magnitude as the former. This can be understood from the previous discussion on the origin of various terms in Eq. 3.3, and in particular what fields contribute to  $V_2$  or  $V_3$ . For this to be true, however, it is important that the orbitals  $u_n$ , and  $u_m$  in the second term have contributions that originate from an atom with a strong spin-orbit coupling. From the point of view of symmetries, another requirement for the second term to be nonzero is that  $u_n$  and  $u_m$  have contributions that have different parity, since  $\mathbf{p}$  is odd in spatial coordinates,  $\mathbf{k} \cdot \mathbf{p}$  is only non-zero when one of the orbitals is odd with respect to a spatial direction and the other even. One example could be a  $p_y$  orbital and a  $s-p_z$  hybridized one, which would be created by the ferroelectricity with electric polarization along the  $z$ -axis (add drawing? add hopping matrix?).

### 3.3 Orbital Rashba Effect

Unlike the purely relativistic Rashba-Bychkov effect, the orbital effect combines strong atomic SOC with the generation of nonzero orbital angular momentum

(OAM) through electrostatic means. This contribution, therefore, is not limited by the small prefactors of Eq. 3.9. As will be explicitly shown below, electric dipole matrix element  $s$  can cause Bloch functions to acquire nonzero OAM when any electric field is present (e.g. from electric polarization), and vice versa Bloch functions with nonzero OAM acquire nonzero electric dipoles between unit cells[13, 12, 4]. This leads to two separate effects.

Firstly, when atomic SOC is included, OAM is unquenched at the high symmetry  $k$ -points. This leads to a correction to the band dispersion that varies linearly with  $\mathbf{k}$ . Secondly, even without including the contribution of the atomic SOC, the OAM of the Bloch functions to appear in a chiral texture as one moves away from the high-symmetry  $k$ -point, similarly to how the relativistic Rashba effect leads to a chiral spin texture. If one then includes the atomic SOC from Eq. 3.3, this linear-in- $k$   $l$  will lead to a linear variation of the energy with either positive or negative slope, depending on the spin orientation.

We now proceed by giving a pedagogical derivation of this mechanism based on a tight-binding model [13, 4].

### 3.3.1 Tight-Binding model

The tight-binding model is defined on a 2D square layer with one atom per unit cell, and four Wannier orbitals on the atom. We assume that these orbitals are gaussians the form  $s(\mathbf{r}, \mathbf{n}) = e^{-\frac{|\mathbf{r}-\mathbf{n}a|^2}{a_0}}$ ,  $p_\alpha(\mathbf{r}, \mathbf{n}) = \alpha e^{-\frac{|\mathbf{r}-\mathbf{n}a|^2}{a_0}}$  with  $\alpha = x, y, z$ , and  $\mathbf{n}$  denoting the unit cell indices  $\mathbf{n} = (n_x, n_y)$ . The reason for choosing gaussians is to make solving the overlap integrals more easy, it does not lead to any qualitative changes to the derivation below. To simplify notation below, we omit  $\mathbf{r}$  and write  $|\alpha^0\rangle = |\alpha\rangle$ . The bare tight-binding Hamiltonian is denoted as  $\hat{H}_0$  and includes the usual hopping parameters due to overlap  $t_{\alpha\beta}^{ij} = \int d\mathbf{r} w_i^\alpha(\mathbf{r})^* (\frac{\mathbf{p}^2}{2m} + V(\mathbf{r})) w_j^\beta(\mathbf{r})$ . To mimick the inversion symmetry breaking in ferroelectric materials (i.e. with a polar space group), an electric field perpendicular to the layer ( $z$  direction) is applied. This allows extra hopping terms associated with  $\hat{H}_{isb} = e(\hat{\mathbf{d}} \cdot \mathbf{E})$ , with  $\hat{\mathbf{d}}$  the electric dipole moment:

$$\langle s | \hat{H}_{isb} | p_z \rangle = 2eE_z \theta_z^n \quad (3.11)$$

$$\langle p_z | \hat{H}_{isb} | p_x(\mathbf{n}) \rangle = eE_z \theta_z^n n_x \quad (3.12)$$

$$\langle p_z | \hat{H}_{isb} | p_y(\mathbf{n}) \rangle = eE_z \theta_z^n n_y \quad (3.13)$$

with  $\theta_z^n = -ae^{-\frac{1}{2}\left(\frac{a|\mathbf{n}|}{a_0}\right)^2} \frac{\pi^{\frac{3}{2}}}{16\sqrt{2}}$ , other terms of  $\hat{H}_{isb}$  are zero. Fig. 3.3 shows pictorially how these terms arise from the electric dipoles between the shifted orbitals.

Solving the tight binding model for  $k = 0$ , one can treat  $\hat{H}_{isb}$  as a perturbation on  $\hat{H}_0$  due to the smallness of  $E_z$ , leading to a hybridization between the  $s$  and  $p_z$  orbitals:

$$|\tilde{p}_z\rangle = |p_z\rangle + \frac{\langle s | 2eE_z \theta_z^n | p_z \rangle}{\varepsilon_z - \varepsilon_s} |s\rangle \quad (3.14)$$

$$|\tilde{s}\rangle = |s\rangle + \frac{\langle p_z | 2eE_z \theta_z^n | s \rangle}{\varepsilon_s - \varepsilon_z} |p_z\rangle, \quad (3.15)$$

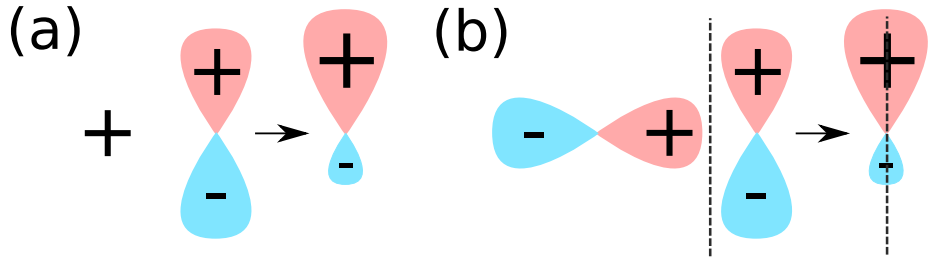


Figure 3.3: Overlap dipoles. (a) Dipole between  $s$  and  $p_z$ , (b) Dipole between shifted  $p$  orbitals, the dashed line signifies a unit cell boundary.

where  $\varepsilon_s = \langle s | \hat{H}_0 | s \rangle$  and  $\varepsilon_z = \langle p_z | \hat{H}_0 | p_z \rangle$ . In order to proceed, we only treat the important kinetic energy part of  $\hat{H}_0$  and rewrite it in terms of this hybrid  $\tilde{p}_z$  orbital in the central unit cell and the shifted  $p_x, p_y$  orbitals, leading to:

$$\langle \tilde{p}_z | \hat{H}_0 | p_x(\mathbf{n}) \rangle = \frac{2eE_z\theta_z^n}{\varepsilon_z - \varepsilon_s} \langle s | \frac{-\nabla^2}{2} | p_x(\mathbf{n}) \rangle \quad (3.16)$$

$$= \frac{4eE_z(\theta_z^n)^2}{\varepsilon_z - \varepsilon_s} n_x (-5 + a^2 |\mathbf{n}|^2) \quad (3.17)$$

$$\langle \tilde{p}_z | \hat{H}_0 | p_y(\mathbf{n}) \rangle = \frac{4eE_z(\theta_z^n)^2}{\varepsilon_z - \varepsilon_s} n_y (-5 + a^2 |\mathbf{n}|^2) \quad (3.18)$$

To construct  $\hat{H}_0(\mathbf{k})$  and  $\hat{H}_{isb}(\mathbf{k})$ , one can Fourier transform the Wannier Functions:

$$|\alpha(\mathbf{k})\rangle = \frac{1}{\sqrt{N}} \sum_{\mathbf{n}} e^{i\mathbf{k}\cdot\mathbf{n}} |\alpha(\mathbf{n})\rangle \quad (3.19)$$

i with  $\alpha$  one of the aforementioned orbitals,  $\mathbf{k}$  written in terms of crystalline coordinates  $(\frac{2\pi}{a})$ , and  $N$  denoting the total amount of unit cells in the material. This results in:

$$\hat{H}_0(\mathbf{k}) + \hat{H}_{isb}(\mathbf{k}) = \sum_{\mathbf{n}} e^{i\mathbf{k}\cdot\mathbf{n}} (\hat{H}_0(\mathbf{n}) + \hat{H}_{isb}(\mathbf{n})) \quad (3.20)$$

$$= \sum_{\mathbf{n}} i \sin(\mathbf{k} \cdot \mathbf{n}) (\hat{H}_0(\mathbf{n}) + \hat{H}_{isb}(\mathbf{n})) + k\text{-even terms}, \quad (3.21)$$

keeping only the  $\sin(\mathbf{k} \cdot \mathbf{n})$  part of the exponent since the  $\cos(\mathbf{k} \cdot \mathbf{n})$  part does not result in linear-in- $k$  terms, in the small  $\mathbf{k}$  expansion below we keep only these linear-in- $k$  terms.

If we then assume that at  $k = 0$  the Bloch functions are formed from  $p_x, p_y, \tilde{p}_z$  and  $\tilde{s}$  orbitals:  $|\alpha(\mathbf{k} = \mathbf{0})\rangle = \frac{1}{\sqrt{N}} \sum_{\mathbf{n}} |\alpha(\mathbf{n})\rangle$  a perturbation theory for small deviations  $\mathbf{k}$  away from zero can be written down:

$$|\alpha(\mathbf{k})\rangle = |\alpha\rangle + \sum_{\beta \neq \alpha} \frac{\langle \beta | H_0(\mathbf{k}) + \hat{H}_{isb}(\mathbf{k}) | \alpha \rangle}{\varepsilon_{\alpha} - \varepsilon_{\beta}} |\beta\rangle \quad (3.22)$$

Gathering the linear-in- $k$  terms, and assuming  $\varepsilon_p = \langle p_x | \hat{H}_0 | p_x \rangle = \langle p_y | \hat{H}_0 | p_y \rangle$ ,

we find

$$|\tilde{p}_x(\mathbf{k})\rangle = |p_x(0)\rangle + \Theta \frac{ieE_z k_x}{\varepsilon_p - \varepsilon_{\tilde{z}}} |\tilde{p}_z(0)\rangle \quad (3.23)$$

$$|\tilde{p}_y(\mathbf{k})\rangle = |p_y(0)\rangle + \Theta \frac{ieE_z k_y}{\varepsilon_p - \varepsilon_{\tilde{z}}} |\tilde{p}_z(0)\rangle \quad (3.24)$$

$$|\tilde{p}_z(\mathbf{k})\rangle = |\tilde{p}_z(0)\rangle + \Theta \frac{ieE_z}{\varepsilon_p - \varepsilon_{\tilde{z}}} (k_x |p_x(0)\rangle + k_y |p_y(0)\rangle), \quad (3.25)$$

with  $\Theta = \frac{\pi^{5/2}}{256a^3} \left( -16\sqrt{2} + \frac{3a\pi^{3/2}}{\varepsilon_z - \varepsilon_s} \right)$ . Then, using the definition of the OAM operators for  $p$ -orbitals:

$$\hat{L}_x = \begin{pmatrix} 0 & 0 & 0 \\ 0 & 0 & -i \\ 0 & i & 0 \end{pmatrix}, \hat{L}_y = \begin{pmatrix} 0 & 0 & i \\ 0 & 0 & 0 \\ -i & 0 & 0 \end{pmatrix}, \hat{L}_z = \begin{pmatrix} 0 & -i & 0 \\ i & 0 & 0 \\ 0 & 0 & 0 \end{pmatrix} \quad (3.26)$$

we find that,

$$\langle \tilde{p}_z(\mathbf{k}) | \hat{L}_x | \tilde{p}_z(\mathbf{k}) \rangle = -2\Theta \frac{eE_z k_y}{\varepsilon_p - \varepsilon_{\tilde{z}}} \quad (3.27)$$

$$\langle \tilde{p}_z(\mathbf{k}) | \hat{L}_y | \tilde{p}_z(\mathbf{k}) \rangle = 2\Theta \frac{eE_z k_x}{\varepsilon_p - \varepsilon_{\tilde{z}}} \quad (3.28)$$

These expressions for  $\hat{L}$  can be filled into the expression for the atomic SOC  $\hat{H}_{soc} = \lambda \hat{\mathbf{L}} \cdot \hat{\boldsymbol{\sigma}}$  to find the energy for  $|\tilde{p}_z\rangle$ :

$$\varepsilon(\mathbf{k}) = \frac{2\lambda\Theta e E_z}{\varepsilon_p - \varepsilon_{\tilde{z}}} (\mathbf{k} \times \boldsymbol{\sigma}) \quad (3.29)$$

which has the form of Eq. 3.1.

From this qualitative derivation, it is clear that the main reason behind the orbital Rashba effect can be traced back to the observation that Bloch functions with nonzero OAM have electric dipoles that couple to the inversion symmetry breaking electric field. We identified two sources that lead to the effect: the first one comes from the direct overlap dipoles between  $p_x$  and  $p_y$  orbitals, and the  $p_z$  orbital[13], the second is due to the hybridization of the  $s$  and  $p_z$  overlap, and the kinetic energy term between the  $s$  and neighboring  $p_x$  and  $p_y$  orbitals[4]. These two terms are reflected in the two terms that contribute to  $\Theta$ , and lead to a chiral, linear-in- $k$  texture of the OAM. If there then exists strong atomic SOC, this linear-in- $k$  OAM will couple to the spin and result in the final Rashba-like form of Eq. 3.29.

There is one final term that contributes to the linear variation of OAM with  $\mathbf{k}$ , which is only present when there is an unquenching of the OAM at the high symmetry point ( $|k| = 0$ ) due to the atomic SOC ???. This is due to the energy gain from  $\hat{H}_{soc}$  if the material has orbitals that have  $\mathbf{j} = \mathbf{l} + \frac{1}{2}\boldsymbol{\sigma}$ . Similar to the above derivation, we can look at a small- $k$  expansion for orbitals that have nonzero OAM. We can write in general that

$$\langle \alpha | \hat{L}_\gamma | \beta \rangle = i\epsilon_{\alpha\beta\gamma} c_\alpha^* c_\beta \quad (3.30)$$

when  $\alpha, \beta, \gamma$  designate  $x, y, z$ . This means that there has to be at least some admixing of multiple  $p$ -orbitals to get nonzero OAM. This leads to the following expansion of the Bloch functions around the high-symmetry  $|k| = 0$  point:

$$|\psi(\mathbf{k})\rangle = \sum_{\mathbf{n}, \alpha} c_\alpha(\mathbf{k}) e^{i\mathbf{k}\cdot\mathbf{n}} |\alpha(\mathbf{n})\rangle \quad (3.31)$$

$$= \sum_{\mathbf{n}, \alpha} \left( c_\alpha(0) + \mathbf{k} \frac{\partial c_\alpha(\mathbf{k})}{\partial k} \Big|_{\mathbf{k}=0} \right) (1 + i\mathbf{k}\cdot\mathbf{n}) |\alpha(\mathbf{n})\rangle. \quad (3.32)$$

Focusing on the terms that vary linearly with  $k$ , the second term in the  $c$  expansion together with the first term in the exponent expansion is exactly the contribution that was discussed before. The final term for the Orbital Rashba effect originates from combining the first term in the  $c$  expansion with the second in the exponent expansion, leading to the contribution

$$\varepsilon(\mathbf{k}) = \langle \psi(\mathbf{k}) | \hat{H}_{isb} | \psi(\mathbf{k}) \rangle = i \sum_{\mathbf{n}, \alpha, \beta} c_\alpha^*(0) c_\beta(0) \mathbf{k} \cdot \mathbf{n} \langle \alpha(0) | \hat{H}_{isb} | \beta(\mathbf{n}) \rangle \quad (3.33)$$

$$= ieE_z \frac{-\pi^{5/2}}{8\sqrt{2}a^3} (c_x^*(0)c_z(0)k_x + c_y^*(0)c_z(0)k_y) \quad (3.34)$$

$$= eE_z \frac{\pi^{5/2}}{8\sqrt{2}a^3} (L_y(0)k_x - L_x(0)k_y). \quad (3.35)$$

These expressions show us that, due to  $\hat{H}_{soc} = \lambda \hat{\mathbf{L}} \cdot \hat{\boldsymbol{\sigma}}$  and  $\hat{H}_{isb} = eE_z d_z$ , an additional Rashba-like term appears in the energy dispersion.

With the understanding that one can find Rashba like dispersions, coming not from the usually considered purely relativistic, but also from electrostatic mechanisms. We now look at a concrete example that behaves very similar to the above toy model, GeTe.

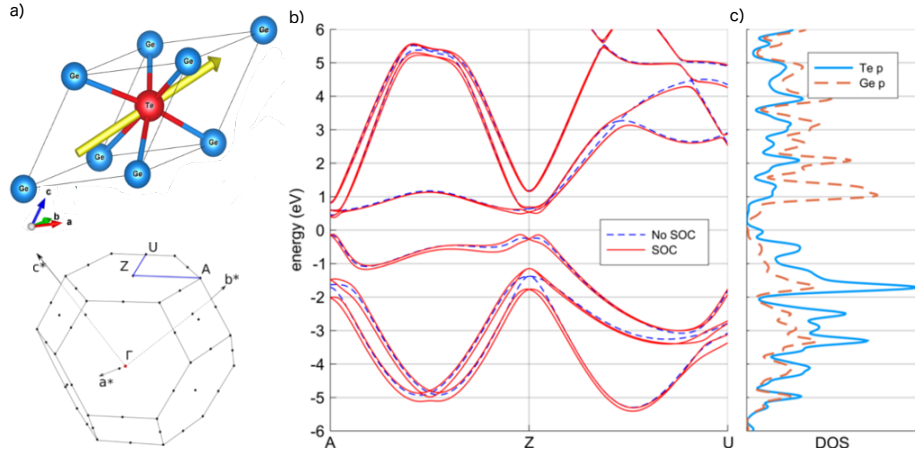


Figure 3.4: (a) Rhombohedral unit cell and Brillouin zone of GeTe, with the polarization direction in yellow. (b) Band structure obtained from a DFT calculation with and without SOC, along the blue path in panel (a). (c) partial DOS for Te and Ge p orbitals computed without SOC.

### 3.4 Overview: Germanium Telluride

The space group of GeTe is  $R\bar{3}m$  (#160 in International Tables), with ferroelectric polarization along the threefold rotation  $z$ -axis caused by an off-centering of the central Te atom [14] as displayed in Fig. 3.4-(a). The valence and conduction bands are formed mostly by  $s$  and  $p$  orbitals from Te and Ge, respectively. This, together with the large spin-splitting in the vicinity of the  $Z$  point [2] as observed from the bandstructure in Fig. 3.4-(b), lends it as a perfect test-case of the above described mechanisms. Moreover, since it is a bulk material, we can rule out the possibility that the relativistic Rashba effects results in a contribution from the existence of possible large potential gradients at a surface. The band structure, presents a distinct large linear spin splitting around the  $Z$  point, resembling the well known Rashba effect. Due to time reversal symmetry, spin-splitting is only present along the  $Z - A$  and  $Z - U$  paths, not the  $Z - \Gamma$  path. The density of states (DOS), displayed in Fig. 3.4-(c), confirms the orbital character of the bands, aluded to earlier.

### 3.5 Methods

To clarify the Orbital Rashba effect in GeTe, we performed ab-initio DFT calculations using the Quantum-Espresso software package[3]. In order to confirm the linear varying OAM even when spin-orbit is not included we performed non-relativistic, as well as relativistic calculations. Both were performed using ON-CVPSP pseudopotentials, with 30 Ry for the energy cutoff, and 160 Ry for the density cutoff. The reciprocal space was sampled using a 10x10x10 and 6x6x6 Monkhorst-Pack grid for the self-consistent and non-self-consistent calculations, respectively, using an energy convergence threshold of  $10^{-7}$  Ry. Afterwards we used the Wannier90 package [11] to perform the Wannierization, using atomic  $s$  and  $p$ -orbitals on both Ge and Te. This provides us with the tools to analyze the real space properties of Bloch functions such as the dipole moment and OAM.

### 3.6 Band structure

The bands we will focus on most are the three topmost valence bands. As seen in Fig. 3.4-(b), these bands have the largest spin-splitting. This suggests that indeed the atomic SOC plays an important role, seen as these bands are comprised mostly of Te orbitals, and SOC is largest on Te. If one were to fit the dispersion of the topmost band to Eq. 3.1, it results in a large prefactor  $\alpha_R \approx 30.7 \text{ eV}\cdot\text{\AA}$  [2]. As discussed before, a more realistic prefactor would be  $\alpha_R = 10^{-6} \text{ eV}$  in the purely relativistic case inside the vacuum.

The last issue with the purely relativistic explanation, which has been confirmed experimentally[9], lies in the orientation of the spin polarization of the split bands. According to Eq. 3.1, the bands should all be split equally and Bloch functions at the same  $k$ -point should have the same spin orientations, since their character does not enter Eq. 3.1. However, as has been shown and will be confirmed by our results below, the orientation depends on the character of the band, more specifically on the value of the total angular momentum  $j$ .

### 3.7 Results and Discussion

The dispersion, OAM, and SAM of the first valence band are shown in the left panel of Fig. 3.6. Confirming our earlier conclusions, we can see that non-zero, linearly varying OAM is formed as we move away from the high-symmetry  $Z$ -point. Moreover, the OAM is perpendicular to both the  $z$ -axis and the  $k$  vector, as it should be from Eq. 3.27, and can also be seen from the panels in Fig. 3.8. This leads e.g. to  $l_y = 0$  along the  $A \rightarrow Z$  path, where only  $k_y$  is nonzero. When atomic SOC is included in the orange and blue graphs, we see the spin-splitting that results from having the spin oriented either along or opposite to the already linearly varying OAM. The unquenching of the OAM at the  $Z$ -point when SOC is included is also clearly visible, together with the resulting change in the slope that originates from the corresponding contribution to the dipole moment Eq. 3.33. This correlation can also be observed in the panel showing the center of mass  $\bar{z} = \int_{\text{supercell}} z|\psi(k)|^2$  of the Bloch-functions, which is proportional to the dipole moment around the same reference point.

When we compare this first valence band with the third valence band, shown in the right panel of Fig. 3.6, we can clearly see the previously discussed issues with the purely relativistic explanation. As stated before, we can note that not only the magnitude but also the sign of the prefactor in Eq. 3.1 is opposite for these two bands, showcased by the size of the splitting, and by the ordering of the spin-up vs the spin-down splitted part. This is because the character of the first and third valence bands are different. The first valence band is mostly coming from Te  $j = \frac{3}{2}$  orbitals, whereas the third valence band is predominantly  $j = \frac{1}{2}$ . This causes the orientation of the OAM and SAM to be along each other in the first band, and opposite for the third, as shown in Fig. 3.8. This then leads to the different ordering of the spin-split bands.

There is one last very interesting feature one can notice from Fig. 3.8 (c) and (f), that is, the switching of the character (and SAM, OAM orientation) of the bands, very close to the  $Z$  point. This is because the crystal field breaks rotational symmetry causing the atomic  $j$  to not be a conserved quantity, i.e.

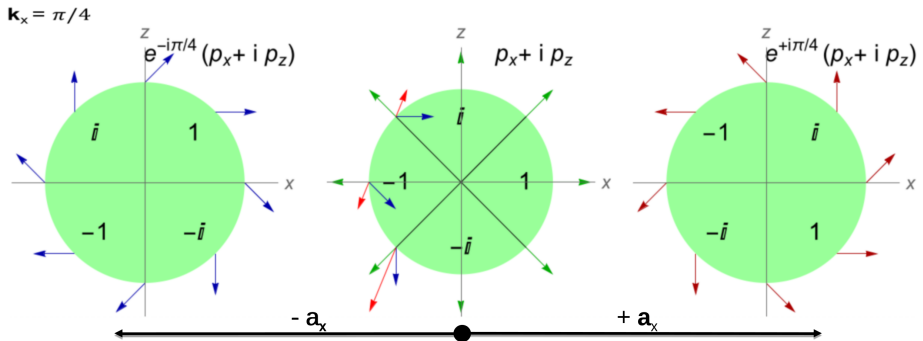


Figure 3.5: Interference between orbitals with nonzero OAM. Three neighboring unit cells are displayed, each with the same  $p_x + ip_z$  orbital (thus having nonzero  $l_y$ ). The wave functions of the left and right unit cells have their phase rotated by the plane-wave part  $e^{ik_x R_x}$ . The amplitude and phase of the wave function are encoded with the length and polar angle of the arrows.

there is a mixing between different atomic  $j$  orbitals, which varies strongly in this very narrow region around  $Z$ .

All these considerations lead to a very nontrivial SAM and OAM texture of the bands as we progress through the BZ.

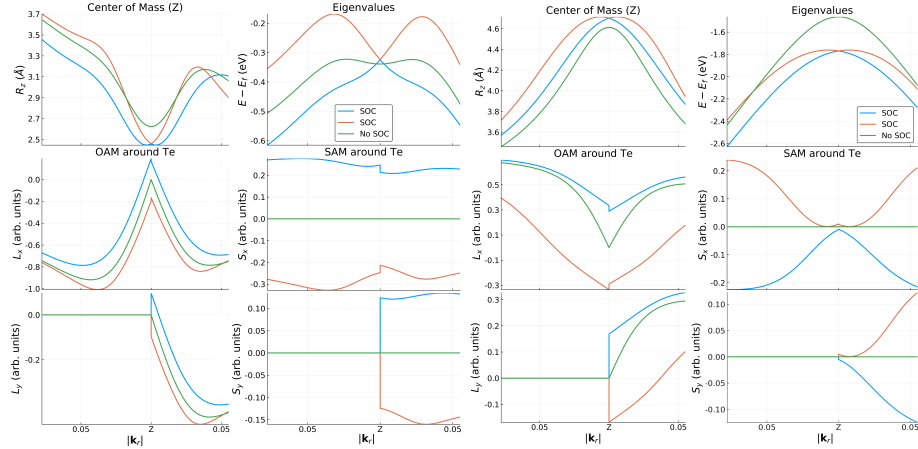


Figure 3.6: Comparison between the real-space observables and energy dispersion in (a) the first and (b) third valence band. The values are plotted in function of the relative distance from the  $Z$  point  $\mathbf{k}_r = \mathbf{k} - \mathbf{k}_Z$ , towards the A and U points. The green graphs denote the values before turning on atomic SOC, whereas the orange and blue graphs denote the two spin-split bands.

### 3.8 Conclusions

We have explored the microscopic origin of the giant Rashba-like spin splitting in the band structure of bulk ferroelectric GeTe with high atomic SOC. We derived the form of the band dispersion in the Wannier representation, that relates the large spin splitting to the intricate interplay between OAM, atomic SOC, the crystal field and the electric polarization. It turns out that the crucial component, which is not present in the relativistic Rashba effect, is the emergence of a nonzero electric dipole of the Bloch functions due to their OAM. The quantitative analysis based on Wannier functions and atomic-centered approximation confirms this mechanism in GeTe. We find a very good agreement between the proposed band dispersion, Eq. (??), and the dispersions of the first and third valence bands, where the effect manifests itself most clearly.

Ultimately, the results suggest that (1) large ferroelectric polarization, (2) high atomic SOC, and (3) highly symmetric environment producing little OAM quenching could be the design rules for new materials with strong Rashba-like spin splitting. These materials could enable spintronic devices with the much needed electric control of spin polarization.

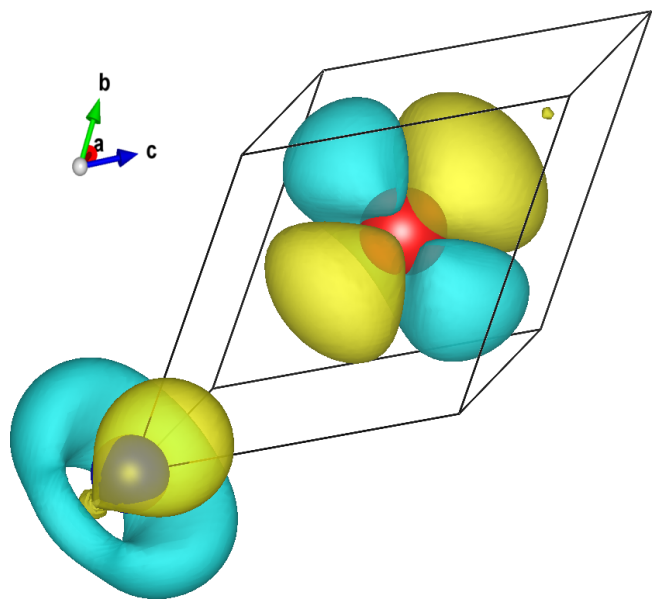


Figure 3.7: The variation of the charge density of the Bloch function of the first valence band  $\frac{\partial|\psi(k)|^2}{\partial k}\Big|_{k=Z}$  away from  $Z$  towards  $A$ . Te and Ge ions are in red and blue, respectively. The charge asymmetry around Ge showcases the nonzero dipole moment along  $z$ , which couples to the local electric field near Ge ion.

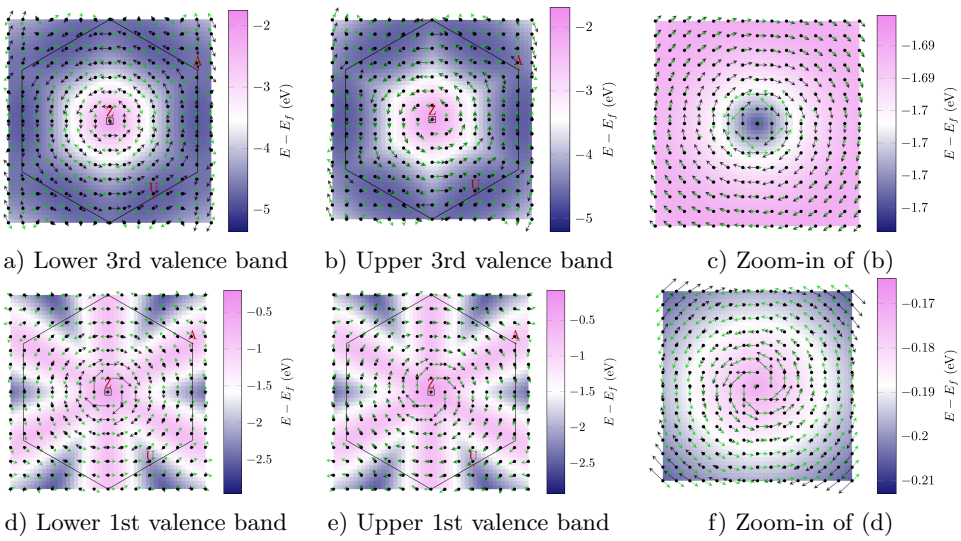


Figure 3.8: OAM and SAM textures around the  $Z$  point in the first and third valence bands of GeTe. The black and green arrows show the OAM and SAM textures, respectively. The length of the arrows was chosen separately for clarity in each figure and should thus not be compared. The color maps signify the energy of the bands, relative to the Fermi level. The small box around the  $Z$  point indicates the area, magnified in panels (c) and (f). In the zoomed figures (c) and (f) one can observe the change or relative orientation between the SAM and OAM when moving away from the  $Z$  point, signifying a change of character between  $j = 1/2$  and  $j = 3/2$ .



# Bibliography

- [1] Supriyo Datta and Biswajit Das. “Electronic analog of the electro-optic modulator”. In: *Applied Physics Letters* 56.7 (1990), pp. 665–667. ISSN: 00036951. DOI: 10.1063/1.102730.
- [2] Domenico Di Sante et al. “Electric control of the giant rashba effect in bulk gete”. In: *Advanced Materials* 25.4 (2013), pp. 509–513. ISSN: 09359648. DOI: 10.1002/adma.201203199.
- [3] Paolo Giannozzi et al. “QUANTUM ESPRESSO: a modular and open-source software project for quantum simulations of materials.” In: *Journal of physics. Condensed matter : an Institute of Physics journal* 21.39 (2009), p. 395502. ISSN: 0953-8984. DOI: 10.1088/0953-8984/21/39/395502.
- [4] Dongwook Go et al. “Surface orbitronics: new twists from orbital Rashba physics”. In: 1 (2016), pp. 1–8. ISSN: 2045-2322. DOI: 10.1038/srep46742. URL: <http://arxiv.org/abs/1611.04674> %0A<http://dx.doi.org/10.1038/srep46742>.
- [5] K Ishizaka. “Giant Rashba-type spin splitting in bulk BiTeI”. In: *Nature materials* 10.7 (2011), pp. 521–526. ISSN: 1476-1122. DOI: 10.1038/nmat3051. URL: <http://dx.doi.org/10.1038/nmat3051>.
- [6] T Jungwirth et al. “Antiferromagnetic spintronics”. In: *Nature Nanotechnology* 11.3 (2016), pp. 231–241. ISSN: 1748-3387. DOI: 10.1038/nnano.2016.18. URL: <http://www.nature.com/doifinder/10.1038/nnano.2016.18>.
- [7] Andrew D. Kent and Daniel C. Worledge. “A new spin on magnetic memories”. In: *Nature Nanotechnology* 10.3 (2015), pp. 187–191. ISSN: 1748-3387. DOI: 10.1038/nnano.2015.24. URL: <http://www.nature.com/doifinder/10.1038/nnano.2015.24>.
- [8] Minsung Kim et al. “Switchable  $S = 1/2$  and  $J = 1/2$  Rashba bands in ferroelectric halide perovskites.” In: *Proceedings of the National Academy of Sciences of the United States of America* 111.19 (2014), pp. 6900–4. ISSN: 1091-6490. DOI: 10.1073/pnas.1405780111. URL: <http://www.pnas.org/cgi/content/long/111/19/6900>.
- [9] J. Krempaský et al. “Surface versus bulk contributions to the giant Rashba splitting in the ferroelectric  $\{\alpha\}$ -GeTe(111) semiconductor”. In: 111 (2015), pp. 1–10. DOI: 10.1103 / PhysRevB . 94 . 205111. URL: <http://arxiv.org/abs/1503.05004> %0A<http://dx.doi.org/10.1103/PhysRevB.94.205111>.

- [10] Marcus Liebmann et al. “Giant Rashba-Type Spin Splitting in Ferroelectric GeTe(111)”. In: *Advanced Materials* 28.3 (2016), pp. 560–565. ISSN: 15214095. DOI: 10.1002/adma.201503459.
- [11] Arash A. Mostofi et al. “An updated version of wannier90: A tool for obtaining maximally-localised Wannier functions”. In: *Computer Physics Communications* 185.8 (2014), pp. 2309–2310. ISSN: 00104655. DOI: 10.1016/j.cpc.2014.05.003.
- [12] Seung Ryong Park et al. “Orbital-angular-momentum based origin of rashba-type surface band splitting”. In: *Physical Review Letters* 107.15 (2011), pp. 1–5. ISSN: 00319007. DOI: 10.1103/PhysRevLett.107.156803.
- [13] L. Petersen and P. Hedegård. “Simple tight-binding model of spin-orbit splitting of sp-derived surface states”. In: *Surface Science* 459.1 (2000), pp. 49–56. ISSN: 00396028. DOI: 10.1016/S0039-6028(00)00441-6.
- [14] K. M. Rabe and J. D. Joannopoulos. “Theory of the structural phase transition of GeTe”. In: *Physical Review B* 36.12 (1987), pp. 6631–6639. ISSN: 01631829. DOI: 10.1103/PhysRevB.36.6631.
- [15] Emmanuel Rashba and V. Sheka. “Symmetry of Energy Bands in Crystals of Wurtzite Type II . Symmetry of Bands with Spin-Orbit Interaction”. In: *Fiz. Tverd. Tela: Collected Papers* 2 (1959), pp. 162–76.

## Chapter 4

# Coupling between spin and strain density waves

### 4.1 Introduction

The coupling between orders

### 4.2 Experimental methods

Before focusing on the theoretical description of the coupling between the SDW and CDW, we take a look at the experimental techniques and results that we are seeking to reproduce. Optical pulses were used to heat up the material, mostly absorbed by the SDW order through photoexcitation. An x-ray free-electron laser (XFEL) is then used to probe the bragg-peaks of the CDW and how they change in time. The need of the XFEL can be attributed to the very short timescales at which the observed behavior is exhibited by the material, with resolutions of a couple femtoseconds being made accessible. The scattering intensity of the bragg peak is directly proportional to the magnitude of the CDW, offering both phase and amplitude information of the oscillation that we study. It is important to realize that the SDW order is not directly accessible through these kinds of measurements, so we are effectively studying the effect of exciting one order parameter through the reaction of the other due to the coupling between them. XFELs also allow for higher peak selectivity (narrow and intense satellite Bragg peaks), such that it allows for measurements performed on thin films even deposited on thick substrates, as was the case in the experiments performed by A. Singer et.al. The thin films offer a clarity in terms of describing the physics of this process, since it leads to a very even excitation of the entire volume, and it causes the order parameters to be homogeneous throughout the material. This absence of topological defects is confirmed by the absence of a widening of the satellite peak associated with the PLD, as compared with the peaks of the material itself. [not sure about this, I actually don't understand what they are talking about in the paper either]. To this end, a 30nm thick Cr film was used in the experiments, harboring seven periods of the SDW perpendicular to the plane. This thinness of the film also decreases

the Neel temperature to 290K, from the bulk value of around 307K. The pulses used to excite the SDW were 40 fs long, with a total intensity of  $2.9 \text{ mJ/cm}^2$ . In the experiments with two sequential pulses the power of the second pulse was roughly half that of the first.

### 4.3 Theory

[some explanation of Peierls instabilities etc, the things that cause the SDW in the first place?]

To understand how modulation of bond lengths changes the magnetic exchange between spins of the constituent ions, it is instructive to recall where the Heisenberg exchange form comes from, namely the Hubbard model:

$$H = \sum_{\langle i,j \rangle} t_{ij} c_{i,\sigma}^\dagger c_{j,\sigma} + U \sum_i U n_i^\uparrow n_i^\downarrow \quad (4.1)$$

where  $\langle i,j \rangle$  denotes nearest neighbors, and  $t_{ij}$  the hopping between them, and  $U_i$  the on-site coulomb repulsion active when the on-site orbital is occupied by more than one electron. In the usual case,  $U \gg t_{ij}$  and thus a Shrieffer-Wolf transformation can be performed to separate the high energy from the low energy subspace. This amounts to performing a second order perturbation theory, allowing the Hubbard model to effectively be rewritten in terms of the on-site spins, leading to the well-known Heisenberg model:

$$H = \sum_{\langle i,j \rangle} J_{ij} \mathbf{S}_i \cdot \mathbf{S}_j, \quad (4.2)$$

with the coupling constant (often referred to as the magnetic exchange)  $J_{ij} = t_{ij}^2/U$ . Since hopping parameters are a result of the overlap between orbitals on neighboring sites, it is clear that they depend on the length of the bond  $r$  between them, i.e.  $t_{ij} \sim r$  to first order. In materials where SDW are formed, this magnetostriction will lead to PLD leading to strain waves.

The geometry that is used in the experiment is such that a microscopic model as described above is unnecessary to describe the essential physics, since the Cr thin film can be considered to be homogeneous throughout the experiment. This allows us to instead adopt a continuum description utilizing a standard Landau theory with two order parameters describing the SDW ( $L$ ) and PLD ( $y$ ) and a coupling between them to describe the magnetostriction.

$$F = \frac{\alpha}{2}(T_L - T_c)L^2 + \frac{\beta}{4}L^4 - gL^2y + \frac{\omega_0}{2}y^2 + \frac{b}{4}y^4. \quad (4.3)$$

The double well potential that leads to the SDW is characterised by  $\alpha$  and  $\beta$ , with the temperature of the SDW given by  $T_L$ , with the critical temperature  $T_c$  below which the phase transition occurs and the SDW order sets in. The coupling between the two order parameters is given by term with  $\gamma$ . Only even orders of  $L$  appear in the energy, since the energy is time reversal even, but  $L$  is time reversal odd. Notice, also, that the PLD order parameter  $y$  by itself would have a zero equilibrium value, the fourth order term with strength  $b$  is only included to provide a better fit to some anisotropic features of the experiment, not to bound the energy as is required if  $y$  would also undergo a second order

phase transition as  $L$ . The equilibrium value of  $y$  will, however, be shifted away from zero due to the force applied to it by the nonzero equilibrium value of  $L$ , a key feature of this model to bear in mind for later.  $y$  is thus a pure slave order parameter.

The temperature of the SDW  $T_L$  is described by a two temperature model, including a time-dependent heat source describing the XFEL pulses, and a bath with non infinite mass and temperature  $T_b$ , meaning that the bath temperature will increase.

$$c_L \dot{T}_L = -k(T_L - T_b) + q(t) \quad (4.4)$$

$$c_b \dot{T}_b = -k(T_b - T_L) \quad (4.5)$$

where  $c_L, c_b$  are the heat capacities of the SDW and the bath,  $k$  the heat transfer rate, and  $q(t)$  signifies the heat injected into the system through the photon pulses, and is modeled by a gaussian  $q(t) = \frac{f}{\tau\sqrt{\pi}}e^{-(t-t_0)^2/2\tau^2}$ , where  $\tau$  denotes the pulse width. The dots signify time derivatives.

In order to solve the time evolution of the system we start by incorporating the free energy given by Eq. 4.3 into the full Lagrangian

$$\mathcal{L} = \frac{m_L(\dot{L} + \gamma_L L)^2}{2} + \frac{m_y(\dot{y} + \gamma_y y)^2}{2} - F, \quad (4.6)$$

where the  $\gamma$  denote the damping parameters for both order parameters. This then leads to the well-known Euler-Lagrange equations given by

$$m_L \ddot{L} = -\alpha(T - T_c)L - \beta L^3 + 2gLy - \gamma_L \dot{L} \quad (4.7)$$

$$m_y \ddot{y} = gL^2 - \omega_0^2 y - b y^3 - \gamma_y \dot{y} \quad (4.8)$$

which we then solve numerically to get the time evolution of both order parameters.

## 4.4 Results

The experimental results we use as a basis to fit our model to are shown in Fig. 4.1. In the numerical model, we found in earlier trials that the dynamics of the SDW order parameter  $L$  is orders of magnitude faster than the ones from the PLD  $y$ , as expected. This can also be seen from Fig. 4.3 since the energy potential is a lot flatter for  $y$  than for  $L$ , leading to a slower time evolution. This difference in dynamics makes it extremely hard to solve the differential equations numerically, we therefore assumed that at each timestep the  $L$  order parameter is in equilibrium in its instantaneous energy potential. This is equivalent to the limit of the mass  $m_L$  in Eq. 4.7 going to zero. The value of  $L$  at a given  $T_L$  and  $y$  can be found by minimizing the Landau free energy 4.3 in terms of  $L$  such that  $\frac{\partial F}{\partial L} = 0$ , leading to:

$$L_0 = \pm \sqrt{\frac{\alpha(T_L - T_c) + 2gy}{\beta}}. \quad (4.9)$$

This eliminates to evaluate Eq. 4.7, instead using Eq. 4.9 to evaluate  $L$  in the partial differential equation for the evolution of  $y$ .

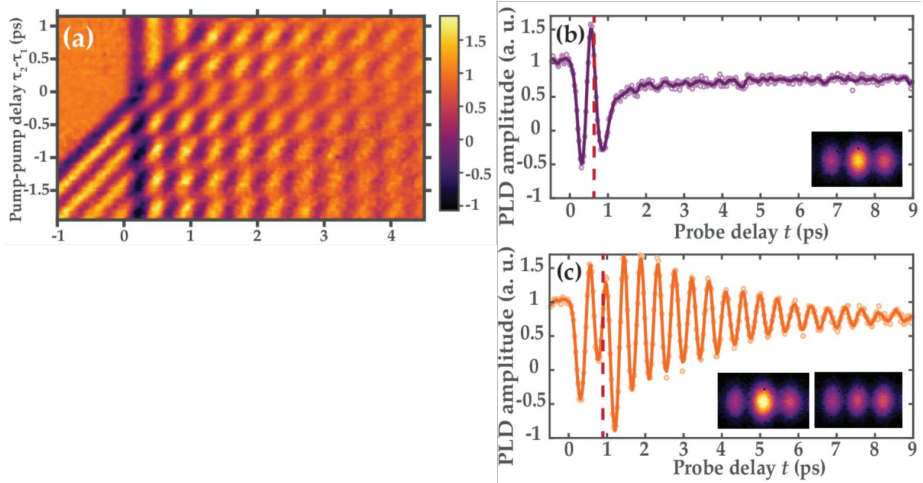


Figure 4.1: Experimental measurements. (a) Heatmap showing different pump-pump delay experiments. Notice the low intensity horizontal band around 0 ps pump-pump delay, where the oscillation amplitude is not at the maximum due to only one big pulse exciting the material and heating it through the phase transition, thus wasting a portion of the energy. The horizontal bands with alternating maximum and minimum magnitudes highlight constructive and destructive interference. (b-c), Magnitude of the strain wave in two extreme control cases, where (b) showcases maximum destructive interference, and (c) close to maximum constructive interference. Solid lines are experimental data (empty circles in figure) smoothed by a Savitzky-Golay filter. b – pump-pump delay of 620 fs, c – pump-pump delay of 845 fs.

We then took eleven representative experiments, which can be thought of as horizontal slices of Fig. 4.1(a), in order to fit the model parameters to get the best total fit across all datasets. The parameters are

$$\alpha = 6039, \beta = 7.97 \times 10^7, g = 0.52, \gamma_L = 25.0, \quad (4.10)$$

$$\omega_0 = 14.1, b = 3.38 \times 10^8, \gamma_y = 0.76, \quad (4.11)$$

$$f = 64.43, c_b = 3.58, c_L = 0.36, k = 1.29, \tau = 0.074 \quad (4.12)$$

The results of this fitting procedure is shown in Fig. 4.2, showing an excellent agreement between the theory and experiment.

To get a deeper understanding of the underlying effect, we look at the evolution of the free energy surfaces for both order parameters, as shown in Fig. 4.3. The characteristic double well potential for  $L \neq 0$  equilibrium is clearly visible, and as expected, when the pulses hit and  $T_L$  increases in the term  $\alpha(T_L - T_c)L^2$  of Eq. 4.3, we see that the potential flattens causing the the minimum of  $L$  to very quickly change, as discussed above. This in turn causes the single-well potential of  $y$  to shift as quickly. The dynamics of  $y$  is orders of magnitude slower than that of  $L$  and due to this instant shift of the energy surface, it will cause an oscillation of  $y$ . While the temperature  $T_L$  decreases again,  $L$  and the minimum of the  $y$  potential shift back towards the original equilibrium position. The oscillation of  $y$  remains for a relatively long time while this shift is occurring

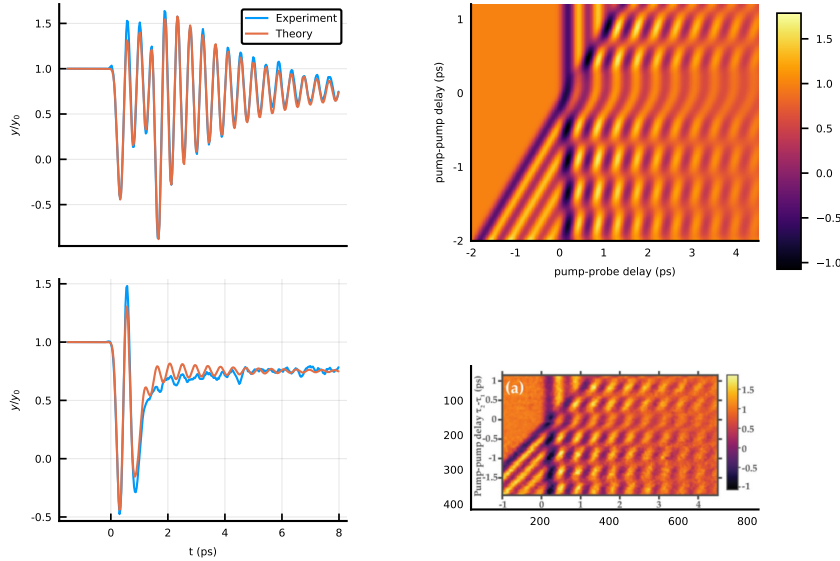


Figure 4.2: Comparison of theoretical fit vs Experiment. (a-b) Two examples of fits to constructive (a) and destructive (b) experiments. (c-d) Comparison of the theoretically generated heatmap (c) with the experimental heatmap (d).

since the damping is not that big (of the order of 4ps). It then becomes clear that if the second pulse can repeat this mechanism while the oscillation of  $y$  is still there, it can be increased or decreased depending on the timing. Having this understanding, let's investigate what the ideal way to excite  $y$  is.

First of all, when the system is relatively close to the phase transition of  $L$ , a small increase of temperature causes a large change in the value of  $L$  as shown through Eq. 4.9, and thus causes a large shift of the potential for  $y$ . It is then important to keep this initial shift of the potential for  $y$  in place until  $y$  crosses the minimum, converting as much potential energy into "kinetic" energy. This requires  $L$  to be heated slightly above the PT, which leads to the largest possible shift of the potential of  $y$ , and the additional temperature of  $L$  above  $T_c$ , together with the non-infinite cooling rate, allows  $y$  to gain the maximum kinetic energy. Since only the size of  $L$  matters for the potential surface of  $y$ , it can only cause a shift in one direction, meaning that, similar to someone pushing a swing, the ideal intervals for the subsequent pulses are close to multiples of the period of  $y$ , if the goal is maximum oscillation amplitude. The amount of periods depends on the cooling rate of  $L$ , this influences how much  $T_L$  can cool back down within one period and thus the size of the maximum shift, since this depends on distance of  $T_L$  from  $T_c$ , and the damping of  $y$  since that is the main source of kinetic energy loss. Taking these understandings into consideration, a high degree of control of the oscillation of  $y$  can be achieved through the intensity, amount and timing of a pulse train applied to the material. To demonstrate this, we went one step further and utilized the fitted model to simulate what pulse train has to be applied to the material in order for the oscillation maxima to follow a given envelope signal. To limit the dimensionality of the manifold of

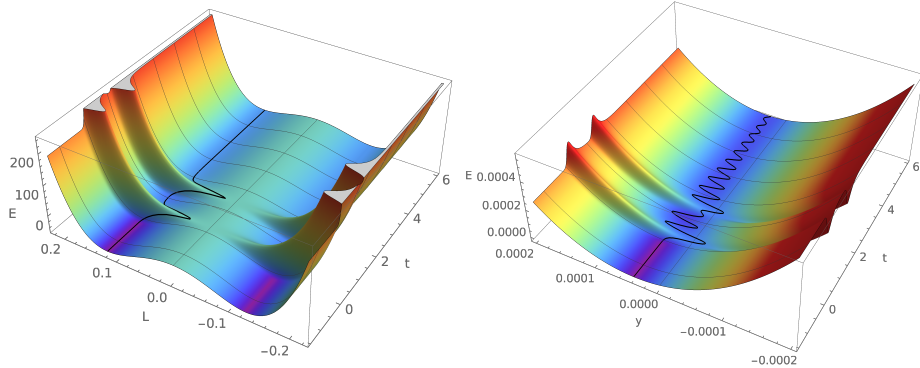


Figure 4.3: Time evolution of the energy surfaces of the order parameters.

possible solutions, we performed the following ruleset:

- Only one fluence can be used per pulse
- Pulses are grouped in sets per period of oscillation
- The first pulse group only has a single pulse, applied 20 fs after the first non zero value of the envelope function, this determines the fluence of each pulse
- The maximum allowed pulses per group is fixed
- The groups are then fitted sequentially, since the later pulses don't influence the oscillation caused by the earlier ones
- If the function is seen to increase during a period, the pulses will be initiated close to the ideal boost location, and if a decrease is required, close to the ideal brake location

Adhering to these rules, we tested this procedure on different envelope functions, showcased in Fig. 4.4. One assumption made here was that the heat capacity of the bath  $c_b$  was increased to infinity, this is done because with the increase of temperature of the bath, the equilibrium position of  $L$  changes and leads to a general downwards slope of the oscillation of  $y$  as see from panel (a-b) of Fig. 4.2.

Having fit the model, we can go one step further and try to fit the PLD oscillation to an arbitrary signal shape. To this end we use the fitted model, and predict the timing of a fixed fluence pulse train that will result in the required shape. The results are shown in Fig. 4.4. This showcases that with an arbitrary pulse train we can achieve indirect, but optimal control of the PLD order parameter.

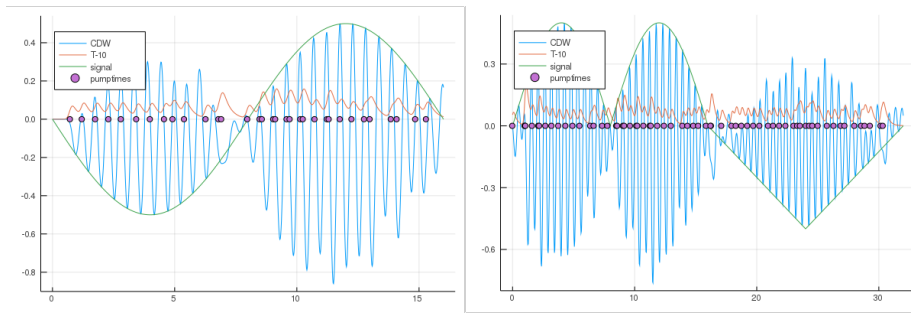


Figure 4.4: Two examples of optimal control. (a) Shows a reproduction of a sinusoidal envelope function, (b) shows the result for more complicated envelope, with an the absolute value of a sinusoidal followed by a half a period of a sawtooth function. The pulse train is highlighted by the purple dots, and the evolution of the temperature of the SDW is given by the orange plot.



## Chapter 5

# Topological Multiferroic switching; coupling between Magnetism and Ferroelectricity in GdMn<sub>2</sub>O<sub>5</sub>

### 5.1 Introduction

Multiferroic materials, where there are multiple ordered structures, have been studied intensely in recent times. The first reason for this is that these orders are usually coupled to some degree, allowing the indirect manipulation of one order by an external perturbation applied to the other. Secondly, this coupling enables a wealth of physical processes to be observed in these materials. Especially materials with relatively low symmetry are a veritable playground to study different effects. In the case under present scrutiny, GdMn<sub>2</sub>O<sub>5</sub>, the magnetic configuration that is present in the system breaks inversion symmetry and leads to a small ferroelectric polarization to show up. With an externally applied magnetic field, we can influence the magnetic order and in turn change the ferroelectric polarization through magnetostriction. Experiments have previously shown exactly this effect, but what was previously missed, is that depending on the angle of the applied magnetic field there are three distinguishable switching regimes. As will be discussed later two of these three regimes can be regarded as two topologically trivial extremes, whereas the third one that lives in the crossover region between these two orders can be regarded as topologically non-trivial in the same sense as a Thouless pump.

### 5.2 GdMn<sub>2</sub>O<sub>5</sub>

Before describing the underlying theory to describe the processes that happen in GdMn<sub>2</sub>O<sub>5</sub>, we focus first on the symmetries that govern the magnetic con-

figuration and which lead to the multiferroicity.

Orthorhombic manganites  $RMn_2O_5$ , with  $R$  being one of the rare earth elements, all have space group  $Pbam$  [Alfonso97a]. Two nonequivalent Mn chains can be distinguished, harboring octahedrally coordinated  $Mn^{4+}$  and pyramidal coordinated  $Mn^{3+}$  ions. The localized spins on these ions couple strongly AFM

As is shown in Fig. 5.1  $GdMn_2O_5$  for a moment on the magnetic unit cell shown in . There are two differently oriented chains of Manganese atoms, distinguished by the light blue lines and polygons. Inside these chains there are both tetrahedrally coordinated ( $Mn^{3+}$ ) and octahedrally coordinated ( $Mn^{4+}$ ) manganese atoms. Due to the Goodenough-Kanamori rules[citation!] these chains are strongly coupled AFM, leading us to assign one AFM order parameter for each ( $L_1$  and  $L_2$ ), this amounts to taking the rigid spin approximation in each chain. However, due to the same rules, the chains also couple AFM between each other. When considering the Mn pentagons formed by the two chains around each of the Gd atoms, it becomes clear that there is a magnetic frustration in the system. This will cause the chains to cant a little to be more perpendicular to each other which can then lead to an energy gain through small canting. This frustration breaks inversion symmetry and leads to the first contribution to the ferroelectric polarization through magnetostriiction. However, due to the spins of the Gd atoms, and their strong AFM coupling to the surrounding Mn atoms, there is a second contribution to the ferroelectricity. This happens because the Gd atom will move towards the closest tetrahedrally coordinated Mn atom in an effort to optimize the super-exchange energy gain with it. These two contributions add up to a polarization of around  $3600 \mu C/cm^2$ , which is tiny compared to proper ferroelectrics, but enormous for multiferroics. Lastly due to the size of the spin from the half-filled f-shell Gd atoms (nominally  $S = \frac{7}{2}$ ), dipolar effects may play a role, and each of the Gd spins inside the unit cell need to be considered separately.

### 5.3 Theory

In light of the above considerations we use a model with two antiferromagnetic order parameters signifying the two orientations of Mn chains, and eight classical spins that describe the different Gd atoms. The Hamiltonian then takes the form:

$$H = \Gamma(\mathbf{L}_1 \cdot \mathbf{L}_2)^2 - \sum_{\alpha} \chi^{-1}((\mathbf{H} \cdot \mathbf{L}_{\alpha})^2 - H^2) \quad (5.1)$$

$$- K_L \sum_{\alpha} (\mathbf{L}_{\alpha} \cdot \mathbf{n}_{\alpha})^2 \quad (5.2)$$

$$+ \frac{1}{2}(g\mu_B)^2 \sum_{i \neq j} \left( \frac{\mathbf{S}_i \cdot \mathbf{S}_j}{r_{ij}^3} - 3 \frac{(\mathbf{S}_i \cdot \mathbf{r}_{ij})(\mathbf{S}_j \cdot \mathbf{r}_{ij})}{r_{ij}^5} \right) \quad (5.3)$$

$$- \sum_i (K_S(\mathbf{N}_i \cdot \mathbf{S}_i)^2 + g\mu_B \mathbf{H} \cdot \mathbf{S}_i) + \sum_{i,\alpha} V_{i\alpha} \mathbf{S}_i \cdot \mathbf{L}_{\alpha}, \quad (5.4)$$

where the first term originates from the competition of the interchain exchange  $J_{\perp}$  and the intrachain AFM exchange  $J_{\parallel}$  [1], with  $\Gamma \sim \frac{J_{\perp}^2}{J_{\parallel}} > 0$  determined by the energy gain on the spin canting, possible when  $L_1$  and  $L_2$  are

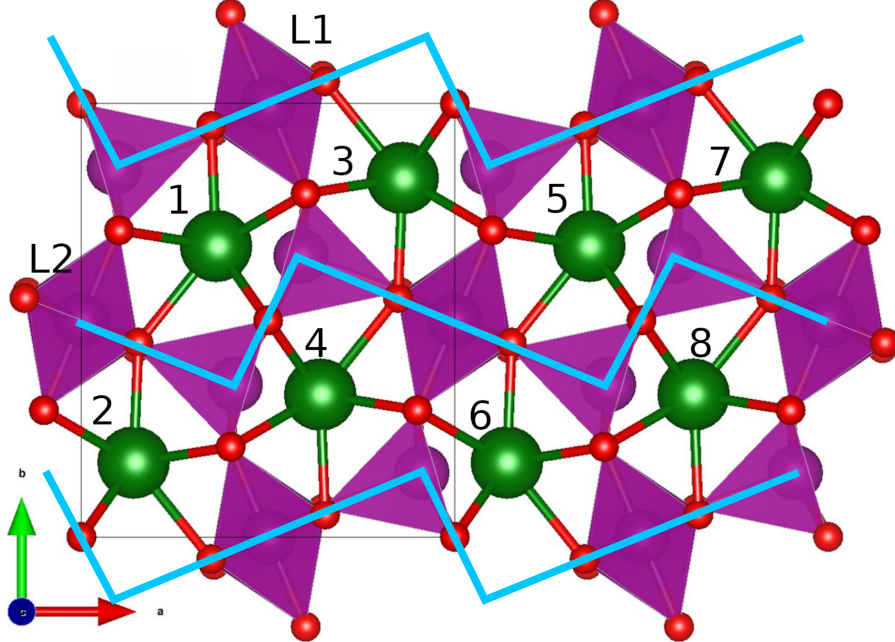


Figure 5.1

not collinear. The term with  $\chi$  represents the gained Zeeman energy when the Mn spins are slightly canted from the purely AFM order inside the chains; terms with  $K_L$  and  $K_S$  refer to easy-axis anisotropy constants of Mn and Gd spins, respectively. Anisotropy axes for  $L_1$ ,  $L_2$  are unit vectors chosen to be aligned with the threefold axes of the tetrahedrally coordinated Mn atoms, i.e.  $n_\alpha = \pm 23.4^\circ$  respectively. The anisotropy axes for the Gd atoms,  $N_i$ , are also unit vectors that alternate as  $\pm 12^\circ$ . The third line describes the dipole-dipole interactions between Gd ions, which were restricted to five nearest neighbors. It was checked that including further neighbors up to 8.5 Å away didn't lead to qualitative changes of the results. The Heisenberg exchange constants  $V_{i,\alpha}$  describe Mn-Gd interactions, where  $V_{i,\alpha} = v_1$  for the exchange constant between the Gd and the nearest (tetragonally coordinated) Mn atom and its chain, and  $v_2$  the exchange with the other Mn chain. The model parameters used here are  $J_\perp = 1.89$  meV,  $J_\parallel = 26.67$  meV,  $K_L = 5.27$  meV,  $K_S = 0.2$  meV,  $v_1 = 3.33$  meV,  $v_2 = 0.15$  meV. The electric polarization  $P_b$ , induced by the Heisenberg exchange striction, is given by

$$\begin{aligned} P_b = & \alpha(\vec{L}_1 \cdot \vec{L}_2) + \\ & (\vec{S}_1 - \vec{S}_5)(\beta \vec{L}_2 + \gamma \vec{L}_1) + \\ & (\vec{S}_2 - \vec{S}_6)(\beta \vec{L}_1 + \gamma \vec{L}_2) + \\ & (\vec{S}_3 - \vec{S}_7)(\beta \vec{L}_2 - \gamma \vec{L}_1) + \\ & (\vec{S}_4 - \vec{S}_8)(\beta \vec{L}_1 - \gamma \vec{L}_2), \end{aligned} \quad (5.5)$$

with the model parameters used to fit the experimental data,  $\alpha = 0.06 \mu\text{C}/\text{cm}^2$ ,

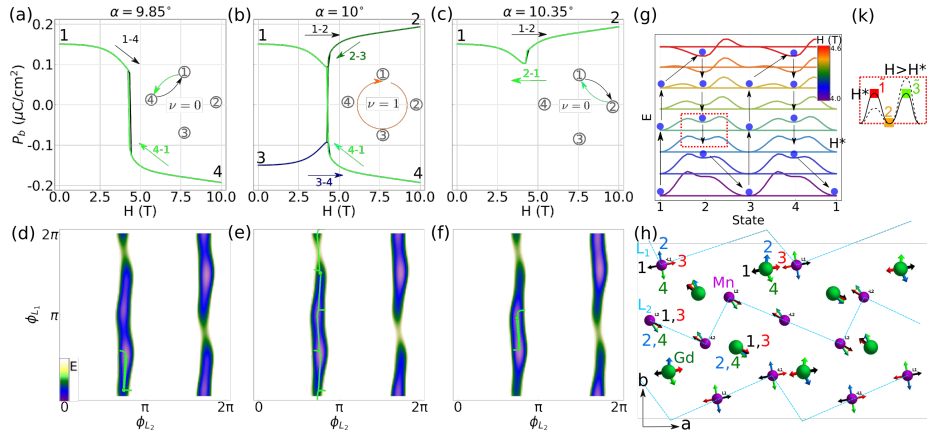


Figure 5.2: (a-c) Evolution of electric polarization  $P_b$  during the magnetic field sweep cycle for various magnetic field orientations. The four states are marked by the numbers, and the switching paths indicated by insets and arrows next to the graphs. The colors are used to indicate sequential sweep branches.  $\nu$  signifies the winding number of each switching regime. (d-f) Trajectories (in yellow) of the AFM order parameter orientations  $(\phi_{L_1}, \phi_{L_2})$  through the field sweep cycles in different regimes. The color map shows the energy landscape at an intermediate field inside the hysteresis region. (g) NEB showing the evolution of transition barriers between states 1,2,3,4 as the magnetic field aligned with magic angle is swept through the hysteresis region. The plots are shifted vertically for clarity. The curve colors encode the corresponding magnetic field strength. The trajectory of the energy minimum due to field sweeps is shown with blue balls and arrows. Coordinated changes of the state energies and barrier asymmetry with magnetic field enable the topological behavior. (h) Spin configurations of the four states, labeled 1...4 in (a). (k) Schematic evolution of the barriers connecting the state 2 to states 1 and 3 away from  $H^*$ . Saddle point states are denoted by  $\tilde{1}$  and  $\tilde{3}$ .

$\beta = 0.04 \mu\text{C}/\text{cm}^2$ ,  $\gamma = 0.06 \mu\text{C}/\text{cm}^2$ . The results are shown in Fig. 5.2

We proceed by identifying the 2 low and 2 high  $P_b$  states in Fig. 5.2(b) as 1,3 and 2,4 respectively. The magnetic configuration of these states is displayed in panel (h) of the same figure. We then perform a nudged elastic band calculation between these states at different magnetic field strengths while remaining in the 4-state hysteresis region, resulting in the evolution of barriers between these states as shown in panel (g), where the color coding is used to denote the magnetic field strength, and the energy graphs are offset for clarity. The arrows and blue balls denote the evolution during the double magnetic field sweep. As expected, there are two degenerate minima at each value of  $H$ , at low field these are located at states 1 and 3, then as the field is ramped up they move to favor states 2 and 4. We see that during the sweep the barriers between the different states evolve asymmetrically. As we start in state 1, when the field is ramped up first the barrier towards state 2 decreases faster than the one towards state 4, causing the system to move from 1 to 2. Then as the magnetic field is lowered, the barrier from 2 to 3 increases slower than from 2 to 1. When ultimately state 2 goes from being metastable to a saddle point, the state spills towards state

3, and so on. In order to try and understand where the asymmetric evolution of the barriers comes from, we look at the particular  $H$ -field strength where the barriers between state 2 and 1, and 2 and 3 are the same height. This is highlighted by the red dashed box around the blue graph. The inset of panel (k) provides a zoom on this situation. The states on top of the barriers are denoted by a tilde over the state towards the barrier is oriented, i.e.  $\tilde{1}$  signifies the state on the top of the barrier from state 2 towards state 1. We then perform a Taylor expansion in terms of  $H$ , around  $H^*$ :

$$F(H) = F(H^*) + \frac{\partial F}{\partial H} \Big|_{H=H^*} (H - H^*) + \dots, \quad (5.6)$$

for each of the states and subtract the result. Using  $\frac{\partial F}{\partial H} = M$  we find

$$F_{\tilde{1}}(H) - F_{\tilde{2}} = (M_{\tilde{1}} - M_{\tilde{2}})(H - H^*). \quad (5.7)$$

[show how to calculate M?] This means that to first order the evolution of the barrier asymmetry is given by the difference magnetization of the states on top of the barriers. Indeed we find that the magnetizations are different from our simulations, confirming that this is at least a part of the reason for the asymmetric evolution of the barriers. Moreover, due to the symmetry of the system, this asymmetry is opposite when the field is swept up, as compared with when the field is swept down. This causes the unidirectional movements through the four states.

## 5.4 Simplified Model

Having found a description for the situation in the complicated material  $\text{GdMn}_2\text{O}_5$  using the model 5.1, one may wonder what the minimal requirements are to have a similar four-state behavior where the spins rotate  $360^\circ$  while the applied field only oscillates along a single axis. We look to the spin configurations of Fig. 5.2(h) for inspiration. It is clear that, although necessary for the  $P_b$  behavior, it seems that the chain with Mn moments most parallel to the applied field does the full rotation, while the other chain merely oscillates around its starting position. The Gd moments seem to follow the behavior of the chain they are most strongly coupled to. This warrants an attempt to explain the observed behavior using only a single chain with its Gd moments. In the particular case where the magic angle is along  $\alpha = +10^\circ$ , we keep  $L_1, S_2, S_3, S_6$  and  $S_7$  as the variables in the model. We also assume that the easy axis of Gd is not that important. This leaves us with the following Hamiltonian, which we will split up in two parts, one with the dipolar terms  $H_{dip}$  and one with all the other terms  $H'$ :

$$H = H' + H_{dip} \quad (5.8)$$

$$H' = J_1(\mathbf{S}_2 + \mathbf{S}_3 - (\mathbf{S}_6 + \mathbf{S}_7)) \cdot \mathbf{L}_1 - g\mu_b(\mathbf{S}_2 + \mathbf{S}_3 + \mathbf{S}_6 + \mathbf{S}_7) \cdot \mathbf{H} \quad (5.9)$$

$$+ K_L(\mathbf{L} \cdot \mathbf{n}) \quad (5.10)$$

$$H_{dip} = \frac{1}{2}(g\mu_B)^2 \sum_{i \neq j} \left( \frac{\mathbf{S}_i \cdot \mathbf{S}_j}{r_{ij}^3} - 3 \frac{(\mathbf{S}_i \cdot \mathbf{r}_{ij})(\mathbf{S}_j \cdot \mathbf{r}_{ij})}{r_{ij}^5} \right). \quad (5.11)$$

Due to the symmetries of this model and the geometry of the material we end up with two copies of one spin in the first half of the magnetic unit cell and one in the second half of the unit cell, with the chain inbetween (see Fig. 5.3).

This causes  $S_2 = S_3$  and  $S_6 = S_7$ , and thus allows us to look at a single one of the two copies. Again keep only nearest neighbor dipolar terms, and assuming no anisotropy for the Gd spins, we end up with

$$H' = 2J_1(\mathbf{S}_3 - \mathbf{S}_6) \cdot \mathbf{L}_1 - 2g\mu_b(\mathbf{S}_3 + \mathbf{S}_6) \cdot \mathbf{H} \quad (5.12)$$

$$+ K_L(\mathbf{L} \cdot \mathbf{n}) \quad (5.13)$$

$$H_{dip} = (g\mu_B)^2 \left( \frac{\mathbf{S}_3 \cdot \mathbf{S}_6}{r_{36}^3} - 3 \frac{(\mathbf{S}_3 \cdot \mathbf{r}_{36})(\mathbf{S}_6 \cdot \mathbf{r}_{36})}{r_{36}^5} \right). \quad (5.14)$$

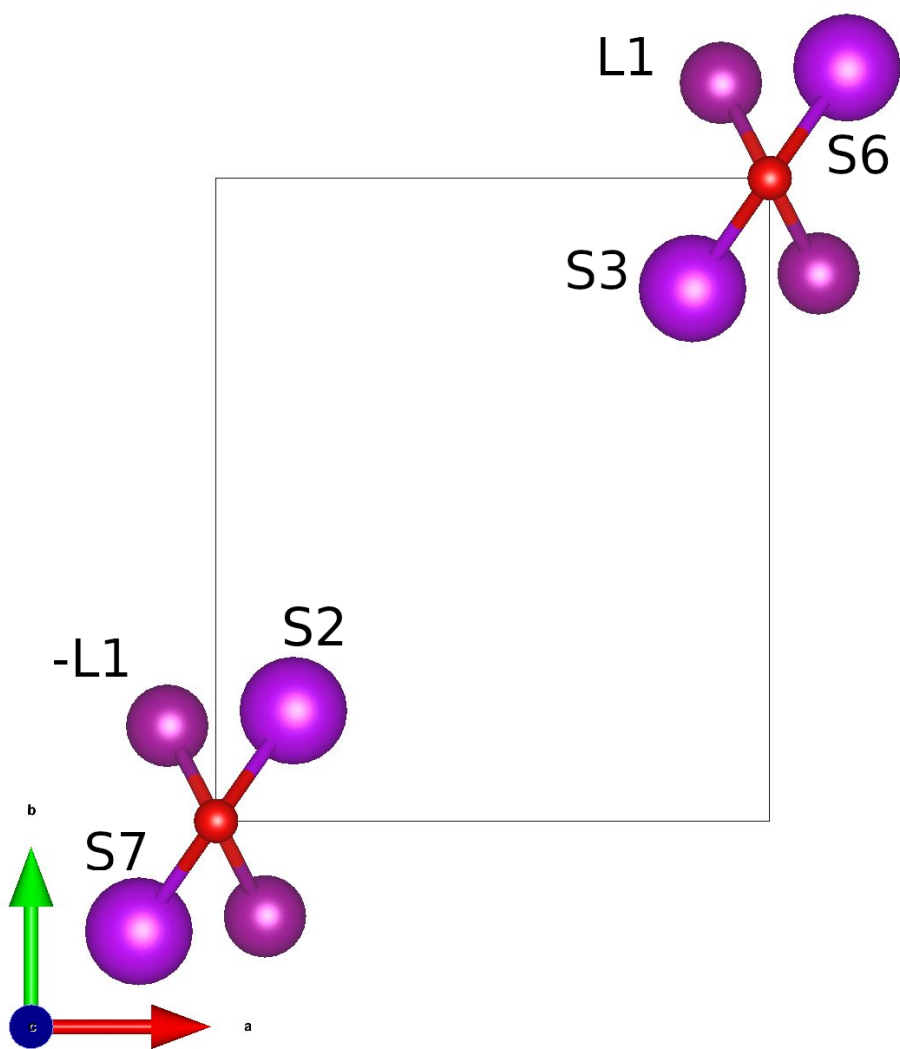


Figure 5.3: Simplified single chain model.



# Bibliography

- [1] A B Sushkov et al. “Electromagnons in multiferroic RMn<sub>2</sub>O<sub>5</sub>compounds and their microscopic origin”. In: *Journal of Physics: Condensed Matter* 20.43 (Oct. 2008), p. 434210. DOI: 10.1088/0953-8984/20/43/434210.



# Chapter 6

## Mechanical softening in Ferroelectric domain walls

### 6.1 Introduction

The study of domain walls in ferroelectric and ferroelastic materials has taken the center stage in recent years. This is because they signify crossover regions between domains where the parent symmetry of the material was broken. These regions therefore often harbor effects that are markedly different from the behaviors found in the domains themselves. Here we investigate mainly  $180^\circ$  domain walls in ferroelectric BaTiO<sub>3</sub> (BTO). These domain walls are purely ferroelectric, i.e. the strain textures accompanying the ferroelectricity (see below for a more in depth discussion) is the same in both domains, separated by the wall. Given this fact it is fairly remarkable that it was observed that these walls are mechanically distinct from the domains they separate. In the case of BTO, they appear softer. After giving an overview of the performed experiments and the results we are trying to describe, we continue with a description of the underlying theory, followed by the numerical results together with a discussion.

### 6.2 Experimental

In order to characterise the stiffness of the material, scanning probe microscopy experiments were performed on single crystal BTO, by the group of Prof. Catalán. More specifically, Contact Resonance Frequency Microscopy (CR-FM) was performed, whereby an Atomic Force Microscopy (AFM) tip is brought into contact with the material, upon which the resonance frequency is measured. The higher the frequency the stiffer is the material in contact with the tip. This allows one to produce a mapping of stiffness the entire crystalline surface where the main limit on resolution is time. This leads to images as shown in Fig. 6.1, where there is a clear contrast between soft areas close to the wall and harder areas inside the domains. The softening of domain walls was previously studied for ferroelastic materials (i.e. materials where the wall separates two domains with different strain textures), where a similar effect was observed [1].

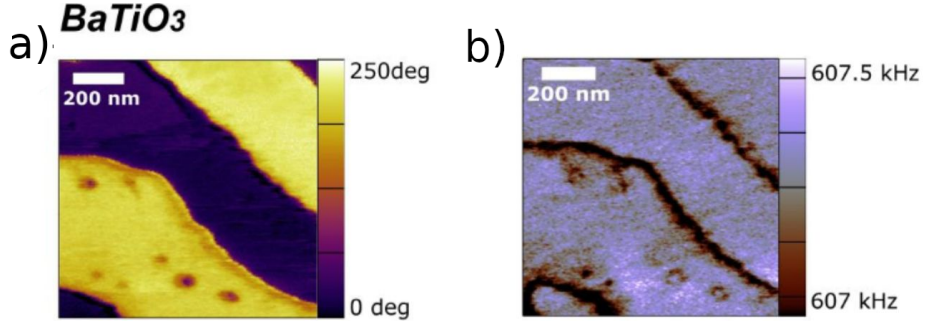


Figure 6.1: Ferroelectric polarization and stiffness maps of the surface of a single crystal of BTO. a) orientation of the ferroelectric polarization, obtained by Piezoresponse Force Microscopy (PFM). b) Mechanical response of the material as measured by CR-FM.

### 6.3 Theory

In order to describe the coupling between the ferroelectric order parameter  $P$  and the strain  $\varepsilon$  we use a Ginzburg-Landau-Devonshire model as described in [2]. The free energy density throughout the material is given by:

$$f = f_L + f_G + f_c + f_q + f_{fl}, \quad (6.1)$$

$$f_L = \alpha_{ij} P_{ij} + \frac{1}{2} \alpha_{ijkl} P_i P_j P_k P_l + \alpha_{ijklmn} P_i P_j P_k P_l P_m P_n, \quad (6.2)$$

$$f_G = \frac{1}{2} G_{jklm} \partial_k P_j \partial_m P_l, \quad (6.3)$$

$$f_c = \frac{1}{2} \varepsilon_{jk} C_{jklm} \varepsilon_{lm}, \quad (6.4)$$

$$f_q = -\frac{1}{2} \varepsilon_{jk} q_{jklm} P_l P_m, \quad (6.5)$$

$$f_{fl} = \frac{1}{2} f_{jklm} (\varepsilon_{jk} \partial_m P_l - P_l \partial_m \varepsilon_{jk}) \quad (6.6)$$

where the indices run through  $x, y, z$ , and einstein summation is assumed. The first term is the Landau free energy for a uniform ferroelectric polarization. Up to sixth order had to be included to bound the energy, since in BTO the fourth order term turns out to be negative. The second term denotes the Ginzburg part, the energy penalty occurred by spatial variations of the polarization.  $f_c$  is the elastic energy density, and  $f_q$  gives the contribution of electrostriction to the free energy. This is the main term coupling the polarization to the strain and causes the domains to be stretched along the polarization [add some panels like in the discussion of the powerpoint]. Lastly we include the flexoelectric contribution,  $f_{fl}$ , since it leads to small but possibly important effects.

The first possible source for the mechanical softening originates from the electrostriction term, and the strain texture it results in. As mentioned before, electrostriction stretches the domains in the direction of the polarization. Since we are investigating  $180^\circ$  domain walls, we can take the main polarization to be  $P_z$ , leading to a stretching of the domains in the  $z$  direction, or equivalently,  $\varepsilon_{zz} \neq 0$  inside the domains. In the domain wall, however,  $P_z^2$  is diminished and

even zero at the center. This then causes  $\varepsilon_{zz}$  to be diminished, but never reduced to zero due to compatibility relations and the elastic coupling to neighboring unit cells. Nonetheless, this will result in an indentation that forms at the location of the domain wall, as shown pictorially in Fig. 6.2(b), and more realistically in (c-d). As it turns out, the strain texture of this indentation stretches out relatively far [actual derivation and formula for this?] from the domain wall. This long-rangedness of strain is a general phenomenon, and depends on the morphology of the strain defect [more indepth on this?]. When the tip is then applied in an area where this strain texture is present, the wall will try to bend towards the tip in order to gain on the displacement. This will thus lead to a relatively big displacement to be caused by applying the tip, making the material appear soft.

Even though the interaction between the pinning potential, Peierls-Nabarro barriers, and electrostatics, with the force applied by the tip is hard to analytically describe, we can make statements about two extremes of the behavior: i) If the force of the tip is large enough, the wall slide towards it, maximizing the possible energy gain from the interaction with the tip. ii) A bending of the wall, where it remains inside the original Peierls-Nabarro potential, but deviates from the equilibrium position. [The situation that happens in the real material is more like a mix between the two, the top part of the wall bends almost completely towards the tip, but it's not moved as a whole because the bottom/bending electrostatics pins it. Can we say that these things are causing the potential for the entire wall to behave like the one we describe below?]

The first case can be ignored because this would mean that in the experiments, the wall would be dragged along the tip since the tip moves at a relatively slow rate, which would lose any contrast between wall and domain during the full measurement. We therefore try to formulate a simple free energy expansion for the second situation, where we assume that the wall at  $x_{DW}$  is pinned by a parabolic potential, and perturbed by a tip applying a force  $F_z$  at  $x_{tip}$ ,

$$E = E_0 - F_z u_z(x_{tip} - x_{DW}) + \frac{m\omega^2 x_{DW}^2}{2}. \quad (6.7)$$

We can expand this equation under the assumption of a small  $x_{DW}$ , i.e. that the wall doesn't move far from the  $x_{DW} = 0$  equilibrium situation. Together with minimizing the energy we obtain  $x_{DW} = -Fu'(x_{tip})/(m\omega^2)$ , with a compliance correction  $\Delta c = u'(x_{tip})^2/(m\omega^2)^2$ . Thus, we can conclude that to maximize the softening, the tip should be applied where  $u'(x_{tip})$  is large, i.e. within the strain variation caused by the above discussed electrostrictive coupling. This part of the effect is pictorially depicted in panel (b) of Fig. 6.2.

## 6.4 Results

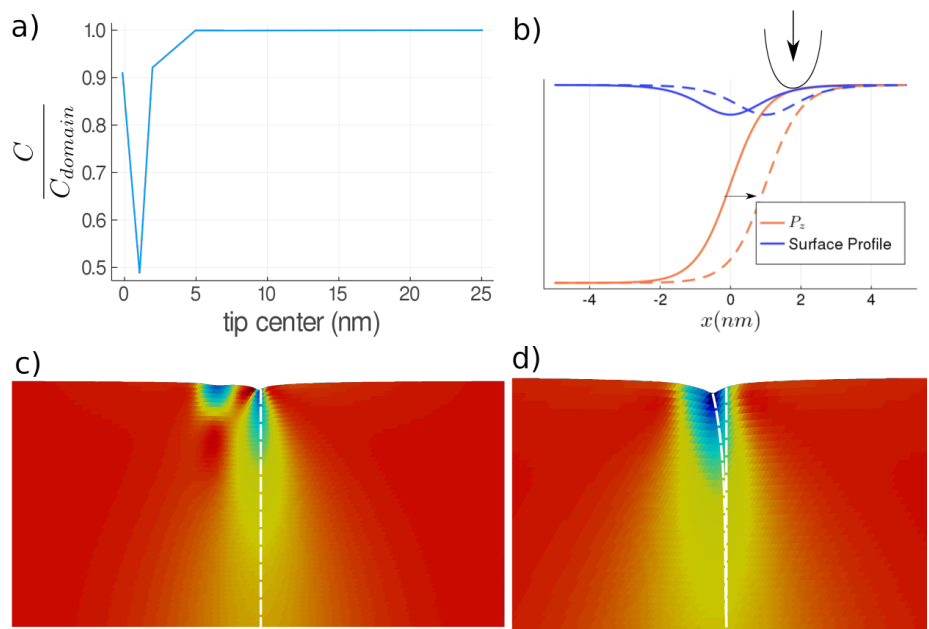


Figure 6.2

# Bibliography

- [1] W T Lee, E K H Salje, and U Bismayer. “Domain wall diffusion and domain wall softening”. In: *J. Condens. Matter Phys.* 15.8 (2003), p. 1353.
- [2] P. Marton, I. Rychetsky, and J. Hlinka. “Domain walls of ferroelectric Ba-TiO<sub>3</sub> within the Ginzburg-Landau-Devonshire phenomenological model”. In: *Phys. Rev. B* 81.14 (2010), p. 144125.



## Chapter 7

# Strong coupling and ultrafast control of charge and spin density waves in elemental Chromium